Investigation of Fatigue and Creep-Fatigue Crack Growth in Alloy 709 at Elevated Temperatures

A Thesis
Presented in Partial Fulfillment of the Requirements for the
Degree of Master of Science
with a
Major in Mechanical Engineering
in the
College of Graduate Studies
University of Idaho

by
Nicholas L. Shaber

Major Professor: Robert Stephens, Ph.D.
Committee Members: Gabriel Potirniche, Ph.D.; Indrajit Charit, Ph.D.
Department Chair: Steven Beyerlein, Ph.D.

December 2018

Authorization to Submit Thesis

This thesis of Nicholas L. Shaber, submitted for the degree of Master of Science with a Major in Mechanical Engineering and titled "Investigation of Fatigue and Creep-Fatigue Crack Growth in Alloy 709 at Elevated Temperatures," has been reviewed in final form. Permission, as indicated by the signatures and dates below, is now granted to submit final copies to the College of Graduate Studies for approval.

Major Professor: _____ Date: _____
Dr. Robert Stephens

Committee Members: _____ Date: _____
Dr. Gabriel Potirniche

_____ Date: _____
Dr. Indrajit Charit

Department Administrator: _____ Date: _____
Dr. Steven Beyerlein

Abstract

The service life of Generation IV nuclear reactors is required to be increased to 60+ years. With increased service life, the likelihood of creep-fatigue failures of structural components increases. Understanding creep-fatigue crack growth behavior is essential for structural applications within nuclear reactors and the power generation industry. Most service conditions involve a combination of creep and fatigue loading. Testing materials in the laboratory is critical to understanding the mechanics of creep-fatigue damage. To date, considerable work in the area of creep-fatigue characterization has taken place on various stainless-steel power plant materials. A recently developed austenitic stainless-steel Fe-25Ni-20Cr (Alloy 709), in consideration for various high temperature reactor applications, has yet to be properly and sufficiently characterized. Characterization of the fatigue and creep-fatigue crack growth properties of Alloy 709 in this study utilized the standard compact tension specimen geometry. The temperature conditions investigated included 550, 600 and 700°C. Proper exemplification of material characterization and consistency of processing techniques was the primary focus of this research. Testing included three separate batches of material that were provided by Oak Ridge National Labs (ORNL). To investigate the effect of prolonged exposure to elevated temperatures, the third batch of material consisted of three aging schedules: as-received, aged 1 and aged 2. Testing conditions under fatigue loading also included loading ratios, R, of 0.1, 0.3, 0.5 and 0.7. Crack growth was characterized in terms of da/dN versus ΔK. For investigation of creep-fatigue crack growth, hold times of 60 and 600s were performed. Fracture surface and crack plane characteristics were investigated with the aid of scanning electron microscopy, electron backscatter diffraction and optical imaging. The primary conclusion from this study indicates minimal sensitivity to loading conditions. Under creep-fatigue loading, creep crack growth was minimal at lower hold times. At a hold time of 600s, there was an increase in crack growth rate. Fracture surface and crack profile imaging indicated transgranular primary and secondary crack propagation. Crack topography and secondary cracking increased as hold time increased. Material in both aged 1 and aged 2 conditions showed little influence on crack growth rates under any tested loading condition of fatigue crack growth or creep-fatigue crack growth.

Acknowledgments

I would like to thank my graduate professor Dr. Robert Stephens and fellow research members in providing me the opportunity to attain a well-balanced and productive graduate experience. I want to thank the Department of Energy – Nuclear Energy University Programs for supplying funding for my time as a research assistant and the funding for the research materials in association with Oak Ridge National Labs. A final thanks to my family and friends, with special thanks to my loving wife Kennadie for her constant encouragement and support.

Table of Contents

List of Figures

List of Tables

Nomenclature

a	crack length
A	secondary creep Norton constant (power law)
A_{nom}	nominal Area
B	specimen thickness
B_n	net specimen thickness
C(T)	compact tension specimen
C_t	time-dependent fracture mechanics parameter
$(C_t)_{avg}$	time average value of C_t
$(C_t)_{ssc}$	value of C_t in the small scale creep regime
C*	steady state creep fracture mechanics parameter
c	load shedding gradient used for ΔK controlled testing
CFCG	creep fatigue crack growth
CCG	creep crack growth
da/dN	fatigue crack growth rate
DCPD	direct current potential drop
E	Young's modulus
FCG	fatigue crack growth
K	stress intensity
K_{max}	maximum stress intensity in a cycle
K_{min}	minimum stress intensity in a cycle
K_{open}	crack opening stress intensity
ΔK	stress intensity range
ΔK_{eff}	effective stress intensity range
N	number of applied cycles
n	Norton creep exponent constant
P	applied load
R	stress ratio (ratio of minimum to maximum load)
SFR	sodium fast reactor
t	specimen thickness
W	specimen width
σ_{ys}	yield strength

1. Introduction

The power industry is continually growing and pushing the bounds of current structural materials; the nuclear power industry is one such industry. Generation IV reactor designs are expected to maintain a service life of 60 or more years. With the increase in service life, fatigue and creep-fatigue failures are of even greater importance in the design of these modern reactors. Understanding the fatigue and creep-fatigue behavior of the applicable structural materials is paramount for safe design. A recently developed austenitic stainless steel, nominally Fe-25Ni-20Cr (Alloy 709), is a potential candidate material for such applications. To date, Alloy 709 has lacked comprehensive laboratory testing and characterization required for material implementation for structural components. The following report discusses the fatigue crack growth (FCG) and creep-fatigue crack growth (CFCG) testing conducted at various temperatures, load ratios, and hold times. The comprehensive analysis of material property repeatability required comparison between multiple batches of material and aged conditions. Funding for this research was provided by the Department of Energy - Nuclear Engineering University Programs, through the project to “Characterize the Creep-Fatigue Crack Growth in Alloy 709 and Predict Service Life in Nuclear Reactor Components”.

2. Literature Review

2.1 Nuclear Reactor Materials

Sodium Fast Reactor (SFR) design concepts are under development for Generation IV (Gen IV) nuclear reactors. The primary challenges for Gen IV reactors are: dimensional stability with high thermal stress capacity, high levels of compatibility with heat-transfer media (sodium coolants), and long term stability/reliability, and ease of fabrication [1]. The SFR design concepts utilize liquid sodium metal for primary cooling, requiring continual operating temperatures of 550°C [2], where peak temperatures can extend well above 650°C. Current materials considered for SFR structural applications are austenitic stainless-steels with high temperature resistance and acceptable irradiation doses [3]. Optimal materials selected for the Gen IV SFR designs will require high creep strengths and sodium compatibility at elevated operating temperatures. The Gen IV reactor designs are set to be in operation for maintained service lives of up to 60 years. Within the 60-year service life, structural components are expected to be subjected to long loading periods along with high frequency vibration resulting from pumps and machinery present within the overall design of the reactor [4]. Current materials under consideration for the SFR designs are represented in Figure 2.1 by a property rank chart [5]. As highlighted in this diagram, Alloy 709 is superior in almost all rankings, second only to a high-temperature ultrafine-precipitate-strengthened (HT-UPS) austenitic stainless in the creep category. Overall, Alloy 709 shows promising material properties for SFR reactor designs.

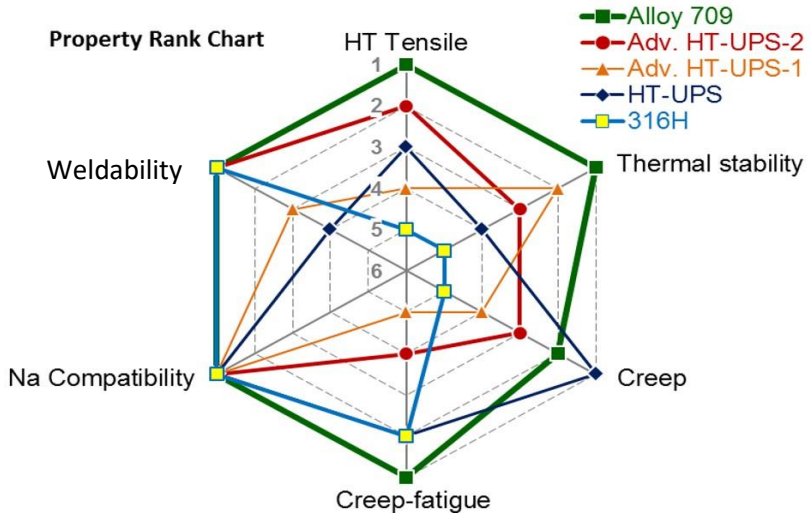

Figure 2.1: Material Considerations for Gen IV SFR designs [5]

2.2 Fracture Mechanics

The importance of fatigue failures and design for fatigue dates back as early as the 1840s with the railway industry and railcar axle failures. Early stress versus life diagrams were developed in the 1860s to characterize a given stress level to the life of a component. Throughout nearly the next decade, numerous tests were conducted around the world investigating the effects of stress concentrations and corrosion effects. It was not until the 1950s that Dr. George Irwin coined the term fracture mechanics. George Irwin and Alan Griffith introduced the stress intensity factor K and the modern principles of fracture mechanics known as Linear Elastic Fracture Mechanics (LEFM) [6]. The loading and extension of cracks is broken down into three modes. Mode 1 is the most common loading case where loading is perpendicular to the crack plane. Modes 2 and 3 result from loading parallel to the crack plane, seen in Figure 2.2. Mode 1 loading is the dominating failure mode experienced under fatigue conditions as the stresses dominate the crack-tip stress field [6].

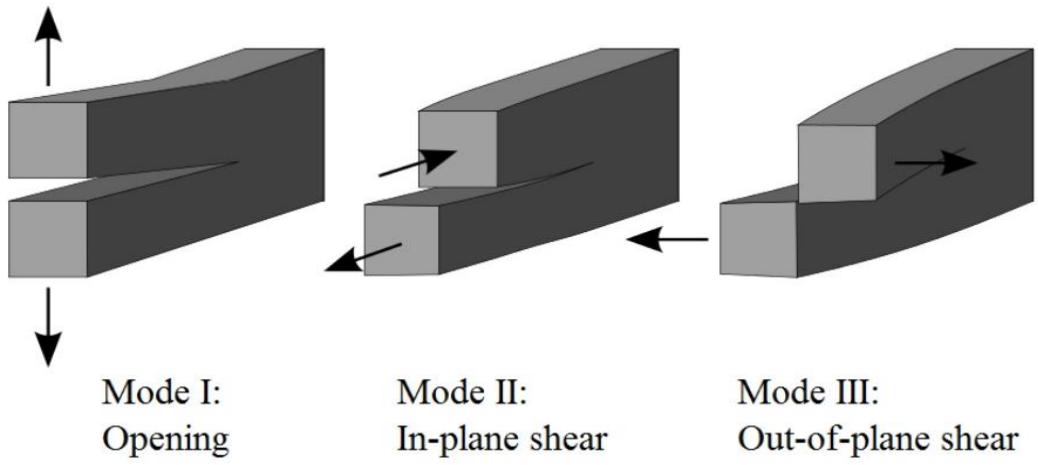

Figure 2.2: Modes of crack extension [6]

The LEFM framework under which crack growth and stresses are characterized has many limitations. The primary qualifying requirement for LEFM characterization regards the size of the plastic zone at the crack tip, requiring the plastic zone to be small in relation to the overall geometry of the specimen. For the standard compact tension, C(T), specimen geometry crack length, a, must satisfy the condition of Equation 1 [7].

$$(W - a) \geq \left(\frac{4}{\pi}\right)\left(\frac{K_{max}}{\sigma_{YS}}\right)^2 \quad (1)$$

where σ_{YS} is the 0.2% offset yield strength at the test temperature, w is the specimen width, a is the crack length and K_{max} is the max stress intensity. LEFM is based on the idea that at the tip of a sharp crack, there will be some plastic deformation that will cause propagation of a crack through the material. The stress intensity factor K is the fundamental parameter used to characterize the stresses at the crack tip. The general form of the stress intensity factor under Mode 1 loading is of the form of Equation 2 [6].

$$K = \frac{P}{A_{nom}}\sqrt{\pi a}\, F\left(\frac{a}{w}\right) \quad (2)$$

Equation 3 is the stress intensity solution for the C(T) geometry used in this study [7]

$$K = \frac{P}{\sqrt{B * B_n}\sqrt{W}} F\left(\frac{a}{W}\right) \quad (3)$$

where $F(a/W)$, is

$$F\left(\frac{a}{W}\right) = \frac{(2+\alpha)}{(1-\alpha)^{3/2}}(0.886 + 4.64\alpha - 13.32\alpha^2 + 14.72\alpha^3 - 5.6\alpha^4) \quad (4)$$

and $\alpha = a/W$, B is the specimen thickness, B_n is the net specimen thickness, w is the specimen width and P is the applied load. Equations 3 and 4 are per the American Society for Testing and Materials (ASTM) standard E-647 for the C(T) specimen and accounts for the axial and bending components applied to the specimen as crack length increases.

The standard method for reporting time-independent FCG data is in terms of crack length per cycle, da/dN, as a function of the stress intensity, K, or more commonly, the stress intensity range, ΔK. The stress intensity range is defined as

$$\Delta K = K_{max} - K_{min} \quad (5)$$

where K_{max} and K_{min} are the maximum and minimum stress intensities of the load cycle. When reducing raw crack length and cycle data to da/dN, ASTM standard E-647 suggest that crack length measurements be made at intervals of no smaller than ten times the crack length measurement precision [8]. The secant method is the recommended technique for calculating da/dN on a point by point basis, Equation 6.

$$(da/dN)_{\bar{a}} = \frac{(a_{i+1} - a_i)}{(N_{i+1} - N_i)} \quad (6)$$

This method is common for both FCG and CFCG test data reduction for time-independent crack propagation in metals [7,9]. The C(T) geometry is ideal for fatigue and creep-fatigue crack growth testing to test a large range of stress intensities as ΔK increases quickly with increasing crack length.

Specimen geometry plays a significant role on the loading conditions when determining fracture toughness and mechanical properties of a material. As seen in Figure 2.3, thin specimens will be in a state of plane stress, while an increasing thickness will approach a plane strain condition. This change in stress state is a result of the transition from a triaxial state of stress to a primarily uniaxial state of stress.

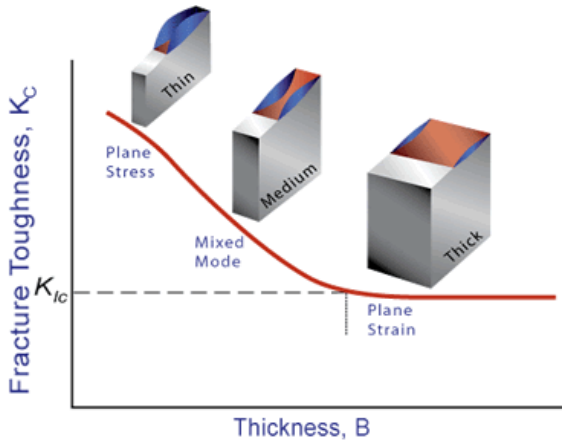

Figure 2.3: Plane Stress vs. Plane Strain loading conditions

2.3 Elevated Temperature Fatigue Crack Growth Testing (FCG)

Elevated temperature testing of metallic materials is critical for numerous modern applications in the power generation industry. Servohydraulic systems are the most common method for testing fatigue properties of materials [6]. Servohydraulic systems are preferred to most other load frame systems due to their versatility, precision and frequency capabilities. A typical servohydraulic system utilizes a proportional servo valve to direct high-pressure fluid to a ram with a feedback control system utilizing either load or displacement feedback. This feedback system provides the capability to attain accurate and repeatable loadings on

specimens and is used widely for FCG testing applications [10]. Modern test systems have the capability to run high-cycle fatigue tests at frequencies greater than 15Hz. To fully understand the mechanical characteristics of a material at elevated temperatures, tests must be run at the elevated temperatures to characterize the mechanical properties under the tested conditions. The test method for determining crack growth rates in materials at elevated temperatures is outlined in ASTM standard E-647 [7]. This standard provides specimen geometry requirements and measurement techniques that are widely excepted. At elevated temperatures, special care must be taken to ensure the environmental testing conditions are maintained throughout the length of a test. The ASTM standards specify temperature variation to remain within ±3°C of the setpoint throughout the length of the testing window. Crack length measurement can be conducted using Crack Opening Displacement (COD) compliance, visual measurement or potential drop (PD) systems [11,12]. Crack growth rates under FCG conditions, as early as the 1980s has shown to change with temperature [13]. Sadananda showed that temperature increases in an air environment had the effect of increasing the crack growth rate of a material for a given stress intensity. This was also seen within a vacuum environment. Furthermore, Sadananda showed that the effect on crack growth rates by temperature is pronounced at crack growth rates on the order of 10^{-5} mm/cycle and below, and that the effect is diminished at higher crack growth rates. These results were found with Type 316 stainless steel specimens in both air and vacuum [13]. The driving factor for the crack growth rate change, as a result of increasing temperature, can be attributed to the decrease in the material's elastic modulus at the given temperature and increased surface oxidation[14].

2.4 Loading Induced Crack Closure

A crack propagates through a material when the driving force at the crack tip is above a minimum level. When a crack is present in a material, there will be a stress intensity, K_{open}, at which the crack opens. When the stress intensity drops below the K_{open} stress level, or sometimes slightly lower, the crack will close. Loading that does not reach the opening stress of the crack tends not to propagate the crack through the given material. Because K_{open} is often greater than K_{min} the effective stress range that drives the crack is not ΔK but rather ΔK_{eff} defined by $K_{max} - K_{op}$ [6]. The loading ratio, R, is the ratio of minimum load to maximum load, P_{min}/P_{max}, or in terms of stress intensity, K_{min}/K_{max}. The R-ratio is the common method in FCG

testing to characterize loading. At higher stress ratios (≈R>0.5), crack closure is limited, i.e. the minimum stress, K_{min}, is equal to or greater than the opening stress, K_{open}, for the material. At lower load ratios, crack closure is more prevalent. In terms of da/dN vs. ΔK, crack closure will manifest as a shift along the ΔK axis. Higher R-ratios had increased crack growth rates compared to lower R-ratios at the same stress intensity ranges. However, if crack growth rates are plotted against ΔK_{eff}, the R-ratio curves will collapse onto one another (low R-ratio curves would shift onto the highest R-ratio curve where no closure is present).

2.5 Creep Brittle vs. Creep Ductile material

Creep crack growth of metals and metal alloys is characterized in one of two ways, as creep-ductile or creep-brittle. Creep-ductile materials accumulate creep deformation ahead of the crack tip at a rate faster than the crack propagates. In these materials, a time dependent parameter such as C* or $C(t)_{avg}$ is favored to characterize the stress at the crack tip. Many high-temperature alloys such as stainless-steel behave in a creep-ductile manner. Creep-brittle materials accumulate creep strains slower or near the same rate as the rate of crack extension. In this case, the stress field at the crack tip can be described using a time-independent parameter such as ΔK [15]. Creep-ductile materials will see much higher creep rates than creep-brittle materials due to the increased size of the creep zone over the cyclic plastic zone [16]. As hold time is increased, the creep zone size at the crack tip will continue to increase faster than the cyclic plastic zone and crack extension rates, resulting in gross plastic deformation of the material and increased crack growth rates. The increased crack growth rate can be broken down into two primary components, a time-independent and a time-dependent crack growth rate.

$$\left(\frac{da}{dN}\right)_{total} = \left(\frac{da}{dN}\right)_{cycle} + \left(\frac{da}{dN}\right)_{time} \tag{7}$$

where $(da/dN)_{time}$ is relative to the hold time of the cycle and is often described as da/dt [17].

At low hold times, it is possible for the creep zone to remain smaller than the cyclic plastic zone and the resulting crack growth rates will not be affected by the hold time [18]. In this case, a creep-ductile material will behave similarly to a creep-brittle material until the hold time is long enough to increase the creep zone size over the cyclic plastic zone.

2.6 Elevated Temperature Creep-Fatigue Crack Growth Testing (CFCG)

CFCG testing, is similar procedurally to FCG testing aside from some modifications. Servohydraulic systems are used to generate the required loading waveform and loading accuracy. CFCG results can be reported in the same manner as FCG data, with da/dN as a function of K or ΔK, although primarily only with creep-brittle materials. When reported in this fashion, the creep effect of the material will manifest in much the same way as temperature effects. For a given temperature, Narasimhachary showed that an increase in hold time translated to an increase in crack growth rate per cycle [17]. More commonly, creep-ductile materials are characterized for CFCG in terms of crack extension per unit time, da/dt, and $(C_t)_{avg}$. This characterization is time dependent rather than cycle dependent. This characterization accounts for crack growth during the hold period of a cycle. $(C_t)_{avg}$ calculation is a function of the load and load-line displacement measured during the hold period. However, load-line displacements during hold times are often small with relation to the displacement resolution; thus, an analytical approach is preferred [17]. The analytical approach for $(C_t)_{avg}$ is:

$$(C_t)_{avg} = (C_t)_{ssc} + C^*(t) \tag{8}$$

where the small scale creep $(C_t)_{ssc}$, is

$$(C_t)_{ssc} = \frac{2\alpha\beta(1-\nu^2)}{E} F_{cr}(\theta, n) \frac{\Delta K^4}{W} \left(\frac{F'}{F}\right) (EA)^{\frac{2}{n-1}} t_h^{\frac{n-3}{n-1}} \tag{9}$$

where n is the Norton Creep Constant, β = 1/3 [19] and

$$\alpha = \frac{1}{2\pi} \left(\frac{(n+1)^2}{1.38n}\right)^{\frac{2}{n-1}} \tag{10}$$

the extensive creep contribution, C*, is given by

$$C^*(t) = \frac{A(W-a)h_1(a/W, n)P_{max}}{\left(1.455 * \eta * B_n * (W-a)\right)^{n+1}} * 10^{-6n} \tag{11}$$

where

$$\eta = \left(\frac{2a}{W-a}\right)^2 + \left(\frac{4a}{W-a}\right)^{0.5} - \left(\frac{2a}{W-a} + 1\right) \quad (12)$$

and h_1 can be found from tabulated values provided in [20].

2.7 Austenitic Stainless-Steel Alloys

Austenitic stainless steels and nickel-base alloys have been the materials of choice for high strength and corrosion resistant applications. Austenitic stainless-steel alloys consist primarily of Fe-Cr-Ni. They are favored for reactor internals due to the need for elevated temperature corrosion resistance. Corrosion resistance is a result of the formation of chromium-containing spinels (i.e., chromite or magnesiochromite), that retard corrosion rates within the material [21]. Nickel is the basic substitutional element used for austenite stabilization; while the equilibrium phases, ($M_{23}C_6$, NbC, TiC, etc.) depend on the proportion of the three elements Fe-Cr-Ni. MX, such as NbC or TiC, and $M_{23}C_6$, such as $Cr_{23}C_6$, precipitates provide increased creep resistance by creating boundaries to dislocation motion. When creep resistance is a primary concern, solution heat treatment is used to dissolve precipitates throughout the microstructure. Subsequent precipitation occurs during creep and increases strength. $M_{23}C_6$ typically precipitates, in order of prevalence, on grain boundaries, incoherent and coherent twin boundaries and intragranular sites [22]. The primary concern when dealing with stainless steel alloys for structural components is the fatigue life and creep strength of the alloy. Most austenitic stainless alloys that are compatible for highly corrosive environments are creep-ductile in nature. Due to the creep characteristics, it is critical to understand crack propagation through the material under various loading conditions.

2.8 Previous Creep-Fatigue Work with Austenitic Stainless-Steels

AISI 316 stainless steels has been the base line for which most new high temperature austenitic stainless steels are compared. AISI 316 is an austenitic stainless steel of nominal composition Fe-17Cr-12Ni. 316 is well known for its superior corrosion resistance to austenitic stainless steels such as 304. Previous work by Michel et al. [23] showed 304 and 316 to be sensitive to loading hold time, Figure 2.4a and 2.4b. Hold times as small as six seconds in both 304 and 316 solution annealed stainless steel increased crack growth rates. When hold times were increased to 60 seconds, both 304 and 316 demonstrated increased

growth rates over the six second hold. The tests were conducted at a temperature of 593°C (1100°F) with a trapezoidal waveform.

Michel et al. also investigated the effect of prolonged exposure at service conditions on material characteristics. An aged condition of 5000 hours (≈7 months) of prolonged exposure at 593°C (1100°F) was investigated. It was determined that at temperatures of 593°C and higher, thermal ageing of the 316 stainless decreased crack growth propagation rates. However, thermal ageing displayed no significant effect on crack growth rates for the other materials investigated: 304, 321 and 348. Also, as temperatures were decreased the effect that the load frequency and load profile had on crack growth rates was decreased.

Both hold time and reduced cyclic frequencies have been observed to increase crack propagation rates at elevated temperatures. The crack growth rates of CFCG loading profiles showed increased crack growth rates over the equivalent frequency FCG load profiles, presented in Figure 2.5 for 316. No difference was observed between FCG and CFCG at equivalent frequencies when tested at lower temperatures. Michel et al. concluded that material behavior and crack growth mechanisms during continuous cycling and hold time at the corresponding frequency were different [23].

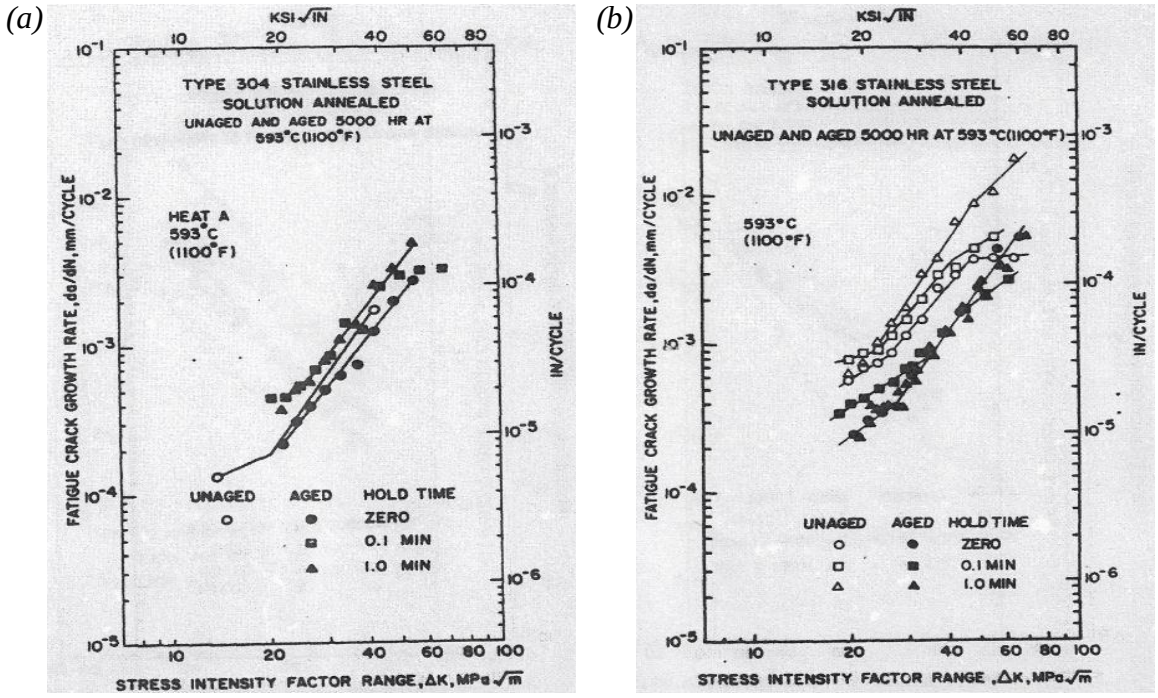

Figure 2.4: 304 and 316 solution annealed stainless steel crack growth rates in as-received and aged conditions [23]

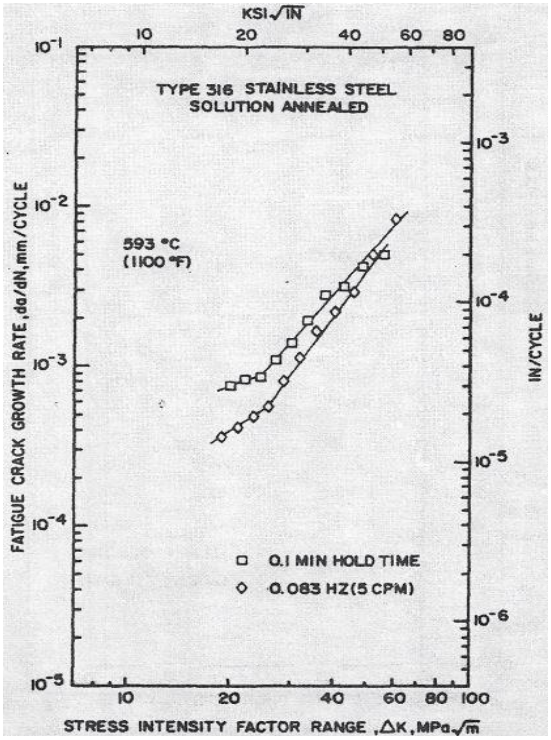

Figure 2.5: 316 solution annealed stainless steel crack growth rates in as-received conditions comparing FCG and CFCG rates [23]

3. Experimental Details

3.1 Material and Specimen Details

The material of interest for this research was Alloy 709: a solution heat treated austenitic stainless steel with nominal composition of Fe-25Ni-20Cr. Alloy 709 was hot rolled then solution annealed at 1100℃. Solution annealing ensured adequate dispersion of precipitates throughout the material microstructure. All material was received for testing from ORNL. Three separate batches were received and processed in a similar manner; the composition of each batch is shown in Table 3.1. Each batch of material was in the form of a plate. The average grain size was 38 ± 3μm. Batch 3 differed from batches 1 and 2 with increased scatter in grain size with banding of smaller and larger grains within the plate, refer to the batch comparison in section 4.1.3 for further details regarding microstructural differences.

Batch/Heat	S	C	Mn	Si	P	Cr	Ni	Mo	N	Nb	Ti	Cu	Co	Al	Be
Batch #1 Heat 011502H	<0.001	0.063	0.88	0.28	<0.005	**19.69**	**25.00**	1.46	0.14	0.23	<0.01				0.0022
Batch #2 Heat 011594	0.0006	0.078	0.9	0.39	<0.005	**19.89**	**25.01**	1.51	0.14	0.25	<0.01				0.0037
Batch #3 Heat 58776-4		0.07	0.91	0.44	0.014	**19.93**	**24.98**	1.51	0.148	0.26	0.04	0.06	0.02	0.02	0.0045

Table 3.1: Material Composition (mass %)

Specimens were machined from the as-received plates such that the rolling direction was parallel to the crack plane. For plate 3, specimens were oriented such that the crack plane was perpendicular to the striated grain structure. Experimental tests were performed at temperatures of 550℃, 600℃ and 700℃. The first batch of material contained three specimens for FCG/CFCG testing, while batch 2 contained 16 and batch 3 contained 48 specimens. Of batch 3, 24 specimens were tested in the as-received condition, while 12 each were used for aged testing at two distinct aging schedules. Specimens were aged at 650℃ for three and six months, respectively. The augmented aging times were meant to simulate 25 and 50 years in service at 550℃. Prolonged service life introduces a σ phase in the microstructure which is detrimental to CFCG characteristics. The known physical properties of Alloy 709, in the as-received and aged conditions is outlined in Table 3.2.

	25°C As-Received	600°C As-Received	600°C Aged 3 months at 650°C	600°C Aged 6 months at 650°C	700°C As-Received	700°C Aged 3 months at 650°C	700°C Aged 6 months at 650°C
Yield Strength (MPa)	251	206	248	N/A	178	249	N/A
UTS (MPa)	624	558	525	N/A	449	423	N/A

Table 3.2: Material Properties of Alloy 709

The specimen geometry selected for the FCG and CFCG testing was the standard compact tension type, C(T) geometry, as outlined in ASTM E-647 with W = 50mm and B = 12.7mm and initial notch length a_n=13mm [7]. For CFCG testing, the C(T) specimen geometry was modified with a 4% 60° V-groove on either side of the specimen along the crack plane; the net thickness was reduced to B_n = 11.68mm. The crack plane groove was intended to prevent crack tunneling and out-of-plane crack growth under creep conditions. A 4% notch was used in favor of the standard 10% notch, because 10% was deemed unnecessary. For the first two batches of material, the initial notch length was a_n = 16mm. For the 3rd batch, the machined notch length was reduced to 13mm to increase precrack length and ensure a uniform crack front. Specimen notch and extensometer edges were machined using wire electrical discharge machining (EDM) in accordance with the ASTM standards for the C(T) geometry [7]. All specimens were precracked at room temperature to an initial crack length a_0=18mm. Specimen geometry is outlined in Figure 3.1. The dimensions chosen are in accordance with ASTM Standard 2760 creep-fatigue crack growth testing [9].

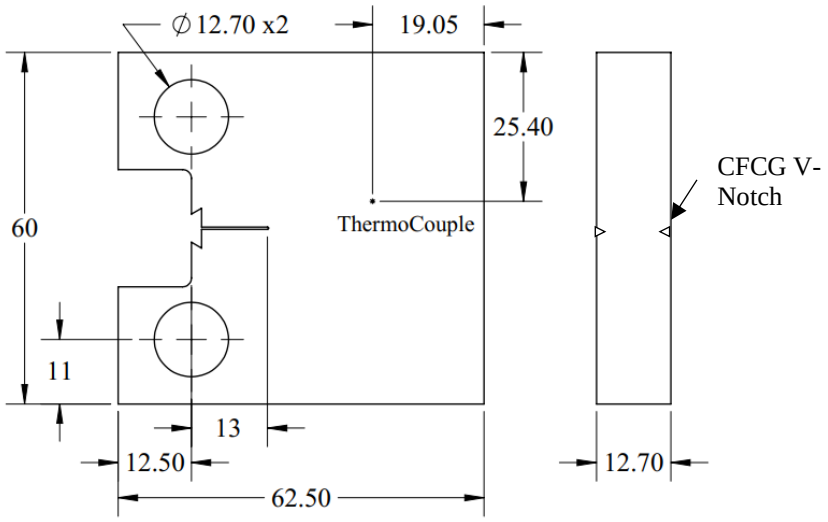

Figure 3.1: Compact tension C(T) specimen dimensions according to ASTM E-647

Starting ΔK levels were typically around ΔK=20 MPa√m while the tests were terminated at a ΔK ≈ 45 MPa√m. A larger range of ΔK values were tested and recorded from a single sample with the development of the Direct Current Potential Drop (DCPD), section 3.5, feedback system that enabled both ΔK controlled increasing and decreasing tests. Utilizing ΔK increasing control, a larger range of ΔK values could be collected for a single specimen. When ΔK decreasing control was utilized, near threshold values were collected. Utilizing ΔK decreasing control, a maximum shedding rate, $c = -0.08\, mm^{-1}$ was used per ASTM standard E-647 [7]. Equation 13 is the load control algorithm used for load shedding as a function of the crack length and thus the stress intensity range ΔK.

$$\Delta K_n = \Delta K_0 e^{c(a_n - a_0)} \tag{13}$$

ΔK_n and ΔK_0 are the current and next stress intensity ranges respectively; a_n and a_0 are the current and previous crack lengths.

Upon test termination, the specimens were cooled to room temperature and cycled at 5 to 15 Hz until failure. Specimen fracture allowed initial and final crack lengths to be measured using fracture surface beach marks and correlated to the measured PD voltage. Crack length was measured at the end of the pre-crack and at the end of the fatigue or creep-fatigue portions of the test by averaging five measurements equally spaced across the crack front.

3.2 Test Frame Retrofit and Verification

As a first step in the research, existing load frames required modification to accommodate temperature-controlled furnaces, high temperature extensometers for COD measurement and DCPD measurement (detailed overview of the DCPD system is explained in Section 3.5). Elevated temperature testing requires the test specimen to be uniform in temperature and maintain a thermal variance of no more than ± 3°C throughout the test duration [24-26]. The furnaces were controlled with Watlow PID temperature controllers (Watlow EZ-Zone®, and Watlow 981 Series); specimen temperature was monitored using K-type thermocouples spot-welded to the specimen above the crack plane on the rear face. The thermocouple location is shown in Figure 3.1. Before any testing, the thermal variance of the specimen was checked at multiple locations to ensure that temperature was uniform across the entire specimen. Two separate test frames were used for all FCG and CFCG testing conducted, as shown in Figure 3.2.

The size of the furnaces and the desired test temperatures required the development of special grips. Due to its high strength at elevated temperatures, grips were machined from Inconel 718. These grips were machined to comply with ASTM E-399 [27] and fit the 12.7mm (0.5in) thick C(T) specimens selected for this testing. The larger of the two frames, Frame 1, was an MTS 312.12 with a load capacity of 100kN (22kips) paired to an MTS TestStar controller with built in ΔK control FCG software.

Frame 1

(a)

Frame 2

(b)

Figure 3.2: Load Frames 1 (a) and 2 (b) with Peripheral Equipment

The FCG software was used for all specimen precrack procedures at room temperature utilizing an MTS 632.02 clip-on extensometer and crack length correlation based on COD as per ASTM E-647.A2 [11], Equation 14,

$$\alpha = \frac{a}{W} = C_0 + C_1 u_x + C_2 {u_x}^2 + C_3 {u_x}^3 + C_4 {u_x}^4 + C_5 {u_x}^5 \tag{14}$$

where

$$u_x = \left\{ \left[\frac{EvB}{P} \right]^{1/2} + 1 \right\}^{-1} \tag{15}$$

Table 3.3 outlines the coefficients used for crack length correlation for extensometer mounting at the load line.

The smaller of the frames, Frame 2, was an MTS 312.11 with a maximum load capacity of 27kN (6kips) utilizing an MTS 458.20 MicroConsole with an accompanying MTS 458.91

Micro-profiler. The MTS 458.20 MicroConsole was calibrated to work with the second load frame.

C0	C1	C2	C3	C4	C5
1.0002	-4.0632	11.242	-106.04	464.33	-650.68

Table 3.3: Compliance coefficients for load line mounted extensometer

3.3 Loading Conditions and Testing Procedure

The two areas of interest were FCG and CFCG. FCG testing was conducted at load ratios of R = 0.1, 0.3, 0.5, and 0.7 utilizing a sinusoidal waveform. R-ratio tests were conducted at frequencies of 15Hz. At R = 0.1, tests were also conducted at a frequency of 0.01667Hz. The 0.01667Hz (60s per cycle) tests were conducted for comparison to the 60s hold time CFCG tests. CFCG testing was conducted at a load ratio of R = 0.1 with a trapezoidal waveform. Predetermined hold times of 60s and 600s were used and the maximum loads were maintained for the duration of the hold. The waveforms are presented in Figure 3.3. Note that waveforms are not to scale with relation to one another.

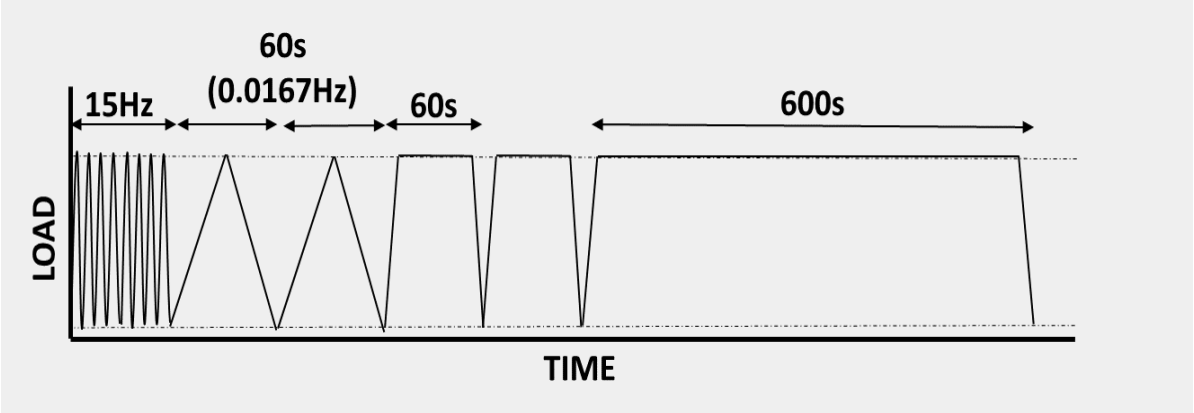

Figure 3.3: Loading waveforms used in FCG and CFCG testing

Throughout the duration of the tests, the minimum and maximum load, loading and unloading compliance, load-line displacement, DCPD voltage, test temperature, and time were monitored and recorded. Visual crack length measurements were also recorded through the furnace window for DCPD measurement validation. Visual measurements were performed using a microscope mounted to a translating stage to monitor crack tip extension. Analog

voltages of all measurements were collected at a rate of 5Hz via a LabVIEW interface. The LabVIEW interface was designed specifically to collect data from both load frames independently. See Figures A.1 and A.2 in the appendix for the LabVIEW coding structure and interface window. A National Instruments (NI) USB-6341 Multifunction DAQ with simultaneous sampling was used to record all voltages. The DAQ had true simultaneous sampling with lane independent 16bit converters to reduce signal noise and channel crosstalk. For Frame 2, DCPD and extensometer voltage were also recorded using the NI USB-6341 during testing. After test completion, signal noise was removed using a running average program that was written in Python. The code is shown in the appendix A.3. Data points were selected at predetermined crack length intervals; ($\Delta a \approx 0.2$mm was typically used) crack length values were used for calculation of crack growth rate and stress intensity factor ΔK.

Frame 1 was integrated more closely to the LabVIEW interface. To conduct ΔK controlled tests, it was desired to have an adequate feedback signal for crack length. Initial testing showed the high temperature extensometer used, an Epsilon E97415, while capable of monitoring crack opening displacement, produced excess noise for the TestStar system to use for crack length feedback at elevated temperature. It was decided to utilize the DCPD system as the feedback/monitoring signal for the TestStar controller. A new sensor was assigned and created within the TestStar software that utilized an input voltage of 0 to 10V calibrated to a crack length of 0 to 50mm. To supply this signal, DCPD voltage was routed through the LabVIEW interface, where it was saved, filtered and then amplified and scaled to produce an output signal to the TestStar controller. This feedback method proved useful in running both ΔK increasing and ΔK decreasing tests. Linear crack length correction was applied to the data after testing based on initial and final crack length measurement from the fracture surface for calculation of ΔK and da/dN.

3.4 Modified Long Hold Time CFCG Testing Procedure

Due to the CFCG behavior of this material, a full-length test for a 600s hold time CFCG was unrealistic. It was estimated that a single test (starting at a $\Delta K = 20$ MPa$\sqrt{m}$, up to a $\Delta K = 40$ MPa$\sqrt{m}$) would have taken approximately 10 months. Due to time restrictions, a modified testing procedure for 600s hold time was developed. The modified testing procedure started at a ΔK of approximately 25 MPa$\sqrt{m}$. The crack was grown under the 600s hold time profile

until approximately 0.5 mm of crack growth was observed, at which point, the crack was propagated to a predetermined ΔK (typical intervals were between ≈2-4 MPa√m) utilizing a sinusoidal waveform at a frequency of 5 to 10 Hz, after which the 600s hold cycling was repeated. This procedure left obvious beach marks on the surface that could be utilized to confirm intermittent hold time growth rates. These beach marks can be seen in Figure 3.4. This modified testing procedure allowed for various ΔK values to be monitored and recorded in a drastically decreased time frame. This test procedure was conducted at temperatures of 600°C and 700°C with batch 2 material and at 700°C with batch 3 as-received, aged 1 and aged 2 material. This modified procedure decreased the testing time to approximately one month for each sample.

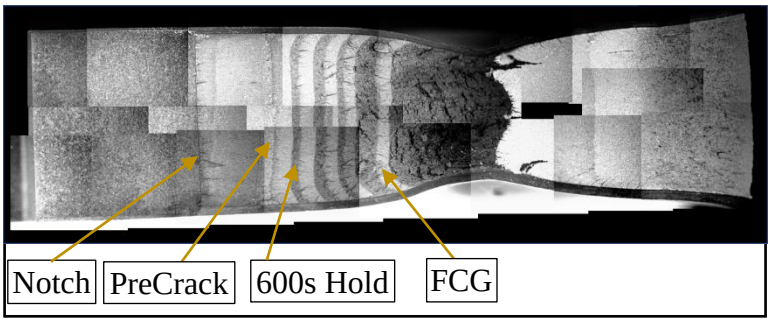

Figure 3.4: Intermittent hold fracture surface mapping

3.5 DCPD Measurement Technique

Direct Current Potential Drop (DCPD) is a common method for monitoring crack length propagation in FCG, CFCG, and CCG testing. ASTM E-647.A3 outlines the use of Electric Potential Difference techniques to monitor crack length [12]. For this testing, direct current was used due to relative ease of setup and availability of equipment. Direct current is supplied to the specimen and the voltage across the specimen is measured. The precision current supply used was a Keithley 2280S-32-6 DC Power Supply, while for output voltage measurement, a Keithley 2182A Nanovoltmeter was used. The combined current supply and voltmeter produced a nanovolt resolution of approximately ±2μV, corresponding to a crack length resolution of approximately ±20μm (0.02mm). Current supply and voltmeter wires were attached to the specimen using spot welded Nichrome 60 wires. 22-gauge and 26-gauge wires were used for the supply and measurement, respectively, and spot welded at position A (supply) and B (measurement) as shown in Figure 3.5.

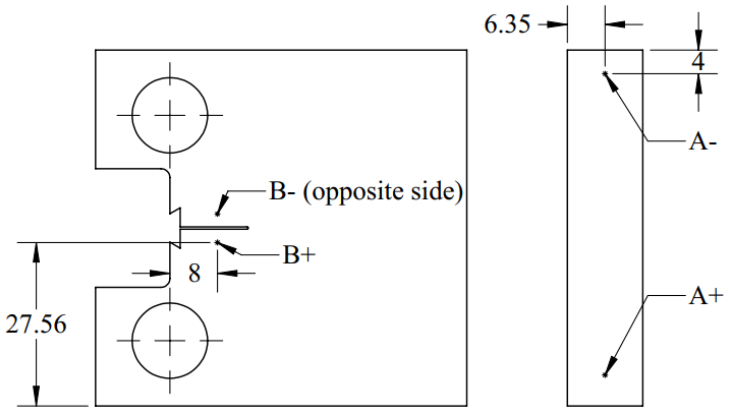

Figure 3.5: DCPD Wire Mounting Locations

A constant current supply of 2 Amps was selected for all tests performed which was sufficient for crack length measurements without voltage measurement error from arcing or crack length shortening. The basis of this DCPD system with numerical analysis and experimental validation is presented in a previous thesis by Philip Malmqvist [28].

3.6 Microscopy

Optical, Scanning Electron Microscopy (SEM) and Electron Backscatter Diffraction (EBSD) imaging of fracture surfaces, profiles, and microstructure were used to compare material batches, loading and aging effects on Alloy 709. For optical imaging, the specimen surface was hot mounted in an acrylic puck using a PACE Technologies TERAPRESS^{TM} and polished using an ALLIED High Tech Products TWINPREP 3^{TM} polishing wheel and stepping grits to a final grit of 5 micron. After polishing, the surface was electro-etched with oxalic acid at 10% by mass with deionized water for 6 seconds. Optical microscopy was conducted using an Olympus PMG-3 light microscope. For SEM imaging, a Zeiss Supra 35 FEG-SEM fitted with a QUASOR^{TM} EBSD system was used. Images were taken at predetermined ΔK values (steps of ΔK = 5 MPa$\sqrt{m}$ from start of crack growth, i.e. 20 MPa$\sqrt{m}$, 25 MPa$\sqrt{m}$, 30 MPa$\sqrt{m}$ …) for comparison to other loading conditions. The fracture surface was inspected at various regions across the thickness of the specimen to ensure an accurate representation of the fracture surface at a given ΔK.

EBSD imaging was obtained after grinding the back side of the crack face until the sample was under 200 µm thick. A Gatan disk punch was used to create 3 mm diameter semi-circles

that were then ion-milled with argon ions using a PIPS II model 695 machine held at an energy of 4 keV for 5 min, 2 keV for 5 min, and 0.5 keV for 8 min. The surface-prepared disks were placed in the SEM. The sample stage was set at an angle of 70° with a working distance of about 16.5 mm. The SEM was operated at an accelerating voltage of 20 kV and run on high current mode. 4 × 4 pixel binning was used to obtain desired resolution.

4. Results and Discussion

4.1 Batch Comparison

Due to the small size of the first plate of material, only three specimens were made, thus only three test conditions were performed: FCG(15Hz) at 600℃ and 700℃ and CFCG(60s) at 700℃. These 3 conditions encompass the loading conditions used for comparison between batches. Due to the small quantity of specimens within batch 1, most of the analysis is between plates 2 and 3.

4.1.1 Crack Growth Rates (Batch Comparison)

Figure 4.1 presents FCG (left) and CFCG (right) data collected from the three batches of material. Comparison of the three batches showed very little differences for both FCG and CFCG loading conditions. Batch 1 tests for both FCG and CFCG showed similar crack growth rates to batches 2 and 3. The primary difference regarding batch 1 was the slope of the da/dN vs. ΔK curve. At both 600℃ and 700℃, the slope of the FCG rate curve for batch 1 was lower compared to batches 2 and 3. For batch 2 and 3, FCG rates overlapped each other substantially; the only difference appearing at low ΔK at 600℃. At ΔK≈20 MPa√m, batch 1 and 3 growth rates are similar and approximately 25% higher than batch 2. As ΔK increased, the fatigue crack growth rates for all three batches, at 600℃, converged at a ΔK≈28 MPa√m.

For CFCG, batch 1 was similar to both batch 2 and 3 for a 60s hold time. There was increased scatter with the batch 1 data at lower ΔK. Batch 2 and 3 demonstrated similar crack growth rates and were only slightly faster than batch 1, less than 5%. For CFCG tests, an increase in crack growth rate scatter at lower ΔK ranges was observed. As a result, a larger Δa was used between data collection for da/dN and ΔK calculation.

For the batch 1 material, variation in the crack growth rate is inconclusive due to the small quantity of samples. With only one test performed for each loading condition in batch 1, it is not possible to conclude if the retarded crack growth rates were anomalous due to measurement error or otherwise. For crack growth rates in batch 2 and 3 materials, no substantial differences in the crack growth rates were seen. Scatter in batch 1 data at low ΔK values for the CFCG loading is attributed to preliminary tuning with the newly developed

DCPD system. Later tests generated more uniform data as use of the DCPD system was improved.

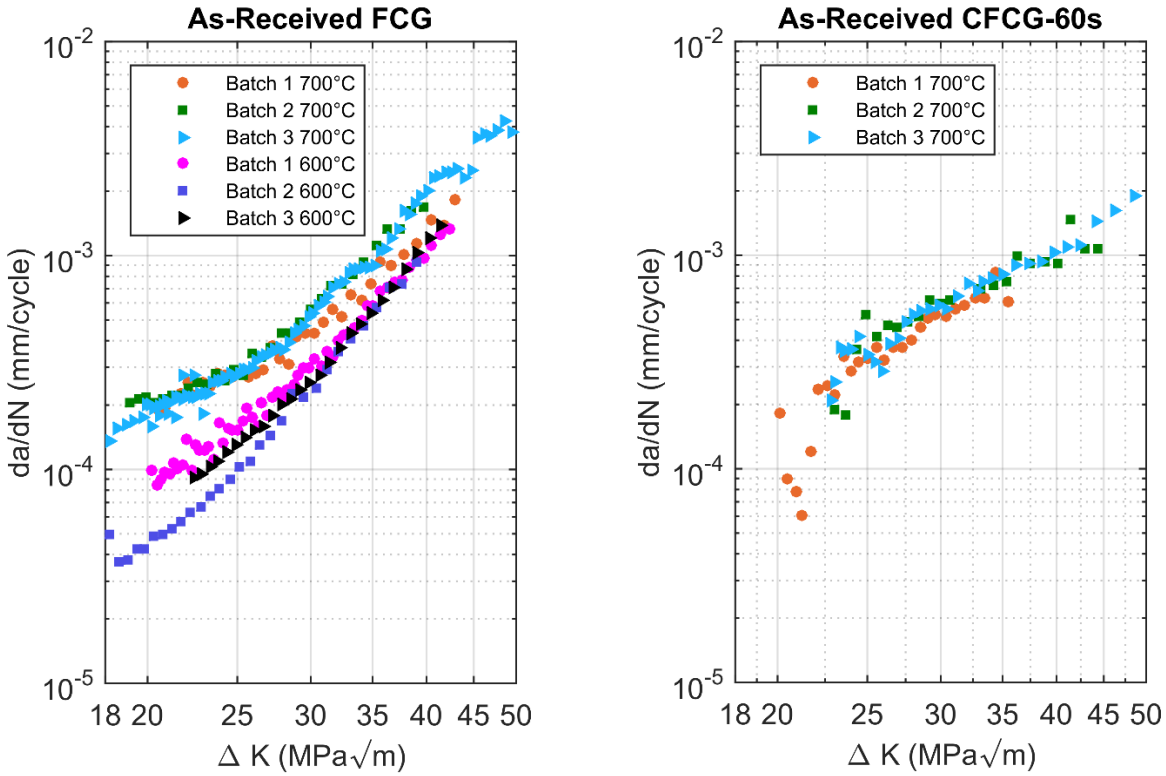

(a) *(b)*

Figure 4.1: Crack growth rates for all batches of material for (a) FCG at a frequency of 15Hz and (b) CFCG with hold time of 60s

4.1.2 Fracture Surface (Batch Comparison)

Specimens under both FCG and CFCG conditions showed some differences in the fracture surfaces. Batch 1 and some batch 2 specimens showed the presence of an oxide on the fracture surface. The oxide was seen at temperatures of 600℃ and 700℃. Figure 4.2 is a representative image of the oxides formed on the fracture surface of early batch 1 and batch 2 specimens.

The oxide was observed in higher concentration near the mouth of the specimen. Post-test inspection of the fracture surface showed a decrease in oxide presence at longer crack lengths. All batch 1 specimens showed the oxide formation regardless of loading conditions. For batch 2 specimens, only the first five specimens showed an oxide presence on the fracture surface for both the FCG and CFCG profiles.

The oxide observed on the fracture surface of the first specimens tested is most likely attributed to initial burn-in of the new furnaces or improper storage of the specimen surfaces before fractography was completed.

Figure 4.2: Fracture surface oxide formation at 700°C under FCG loading, 1kx magnification

4.1.3 Microstructure (Batch Comparison)

The 3 batches of material had small differences in microstructure and chemical composition. Table 3.1 (page 12) outlines the constituent compositions of the three batches with the most notable differences pertaining to batch 3. Batch 3 showed trace amounts of Copper, Cobalt and Aluminum, while none were identified in batches 1 and 2. Batch 3 also showed no Sulfur content and a small increase in Titanium content. When comparing the microstructure of the plates, plates 1 and 2 showed very similar microstructures with an equiaxed grain structure in all plate directions, with an average grain size of 38±3µm. The equiaxed grain structure from plate 1 is shown in Figure 4.3. Figure 4.3 was generated from images of all 3 orientations of the grain structure. The grain structure of batch 1 is representative of plate 2 material as well [29].

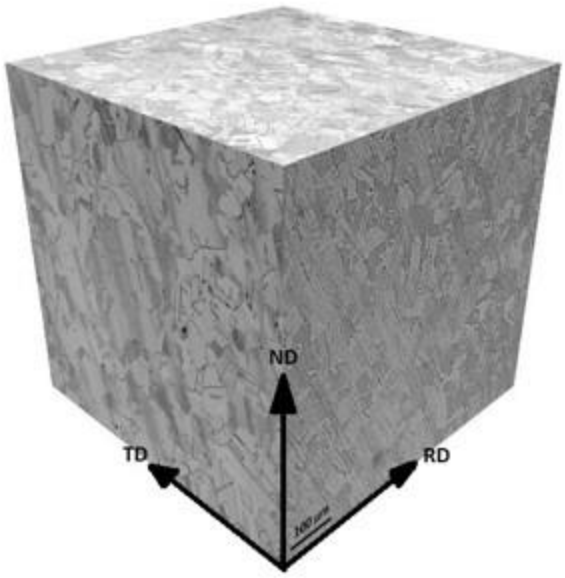

Figure 4.3: Plate 1 Microstructure
(Representative of Plate 2)

Plate 3 material had microstructural differences from that of plates 1 and 2, Figure 4.4. A varying grain size through the thickness of the plate was observed; most notably, on the normal-rolling directions (ND-RD) plane. The rolling-transverse directions (RD-TD) plane shows the banded structure from on end. For batch 3, there was increased grain size variation compared to batches 1 and 2. The grains size of batch 3 had a larger range of grain sizes with a similar magnitude as plates 1 and 2 at 38±6μm. Specimens were machined from the plate with the crack plane oriented perpendicular to the banded grain structure. With the crack plane perpendicular to the banding, crack growth propagated through an average of the grain sizes.

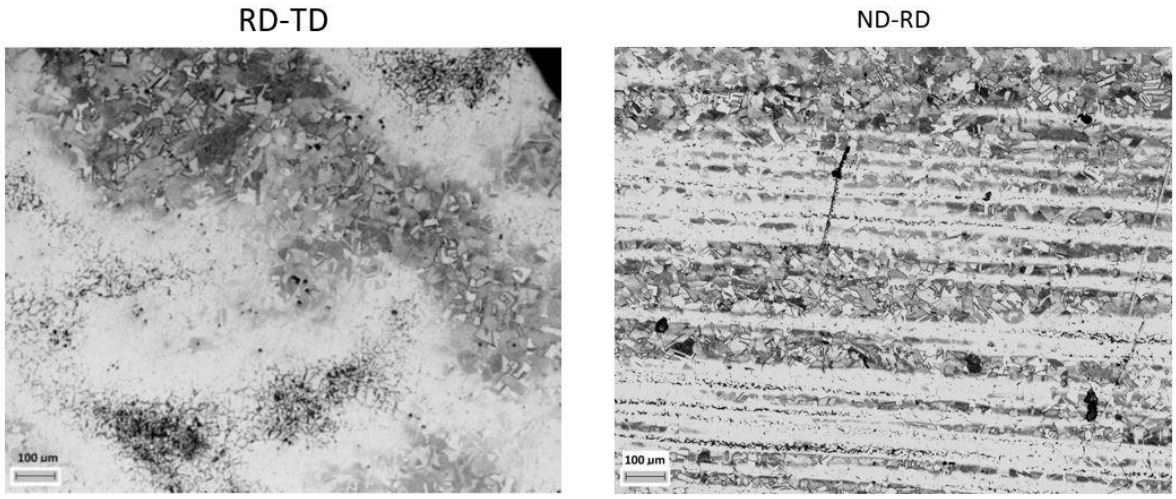

Figure 4.4: Plate 3 Microstructure

Since variation in the microstructure of the as-received material was only seen in the third batch of material, it is reasoned that there was an anomaly with the solution annealing process. Since the third plate of material received was also the largest, it is possible that solution annealing was not achieved to the same level as previous plates of material through the full thickness. There was an increase in the presence of additional constituents in the plate 3 material; however, it was still within set specifications for Alloy 709. For batches 1 and 2, $M_{23}C_6$ precipitates were shown to develop in the microstructure to strengthen the material under creep loading [29]. Overall, while the microstructure showed variations in grain size uniformity, the average grain and microstructural characteristics remained similar. Specimens from the third batch were machined from the ND-RD plane of the plate. Machining specimens from the plate in this manner placed the banded grain structure perpendicular to the plane of crack growth; thus, the crack propagated through an average of the grain structure bands.

Crack growth rates of batch 3 for both FCG and CFCG loading profiles presented no differences. The variation in the microstructure did not appear to have any detrimental effects on either FCG or CFCG rates at the conditions tested.

4.2 Fatigue/Creep-Fatigue Comparison

For the 3 batches of material, a total of 54 specimens were tested. Of these, 15 were tested under CFCG loading, 10 of them with a 60s hold time and 5 of them with a 600s hold time (intermittent procedure). Under FCG loading, a total of 17 specimens were tested at an

R ratio of 0.1 for comparison to CFCG. Of the 17 FCG samples, 2 were tested at low frequency (0.01667 Hz) to simulate equivalent cycle time to the CFCG 60s hold tests. The remaining specimens were tested under various other conditions and are discussed in later sections.

4.2.1 Crack Growth Rates (Fatigue/Creep Fatigue Comparison)

Creep-Fatigue crack growth in Alloy 709 showed only minimal effect on crack growth rates at various temperatures. Figure 4.5 shows CFCG and FCG data from Batch 2 material at 600°C and 700°C. At a hold time of 60s and 600°C, crack growth rates showed no difference compared to FCG over the tested range. For the entire test range of ΔK there is strong overlap of the CFCG rates as compared to FCG. Likewise, at 600°C, the decreased cycle frequency of 0.01667 Hz had no appreciable effect on the crack growth rates where there is again overlap of the FCG (0.01667 Hz) with regard to the FCG (15 Hz). For both the FCG (0.01667 Hz) and 60s CFCG, the tests were started at a higher ΔK in order to minimize overall test time. These results suggest that alloy 709 behaves as a creep-brittle material at temperatures as high as 600°C.

At 700°C, crack growth rates showed some distinction between test frequency and hold time. For CFCG with a 60s hold, there is an increase in crack growth rates at low ΔK relative to the 700°C FCG rates at 15Hz. However, as ΔK increased the crack growth rates began to tail off and crack growth rates became slower relative to the FCG rates. Thus, crack growth rates for the 60s hold CFCG transition from faster than FCG (15 Hz) to slower at a $\Delta K \approx 30$ MPa$\sqrt{m}$. The rate reduction for the 60s hold is a factor of 2 slower than the FCG (15 Hz) loading profile at a $\Delta K \approx 45$ MPa$\sqrt{m}$. When the hold time was increased to 600s, there was again an increase in crack growth rates relative to FCG at low ΔK that decreased at higher ΔK. The crack growth rates of the 600s hold time were greater than the 60s hold times by at most ≈30% over the tested range of ΔK's. The decreased frequency FCG (0.1667 Hz), showed a slight increase in the crack growth rate over the 15 Hz. The 0.1667 Hz loading merge in with the 15 Hz loading by a $\Delta K \approx 35$ MPa$\sqrt{m}$. The gap in data for this test was due to a computer error that temporarily halted data collection.

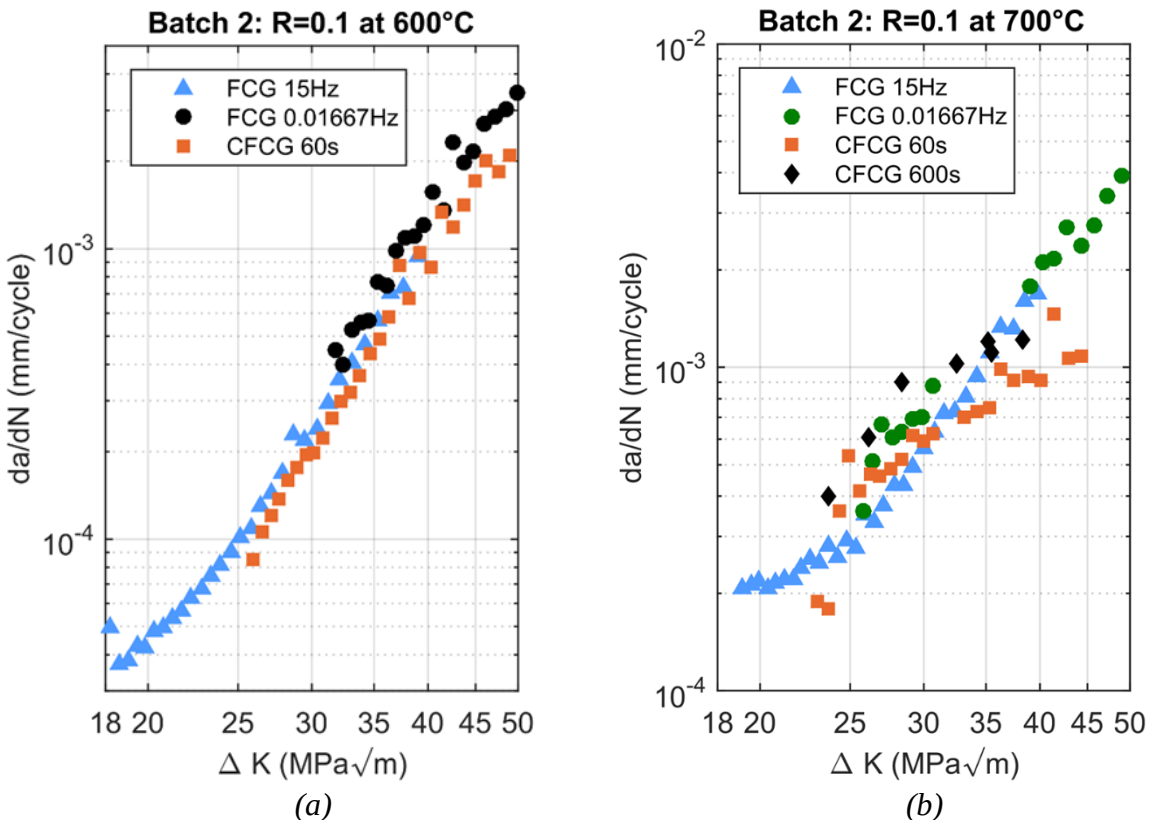

Figure 4.5: Crack growth rates in Batch 2 material at (a) 600°C and (b) 700°C

Between FCG and 60s CFCG the difference in crack growth rates is likely attributed to the increase in secondary cracking. At lower stress intensities, secondary cracking was small and did not hinder crack growth. Thus, at lower stress intensities, $\lesssim$25 MPa$\sqrt{m}$, the crack growth rates are similar or marginally higher between loadings. As the stress level increased, secondary cracking and crack tip blunting was observed. These combine to absorb much of the energy at the tip of the crack to decrease the driving force. The various EBSD scans and fracture surface imaging confirm the increase in depth and severity of the secondary cracking during loading. The decrease in driving force translates into a slower primary crack growth rate with an increase in gross plastic deformation at higher stress levels. This will be discussed in more detail in 4.2.2-4.2.3. Batch 1 and 2 experimental data has shown strong agreement with modeling efforts at the University of Idaho (UI). Modeling of crack growth rates at 700°C for FCG, CFCG (60s and 600s Hold) generate da/dN vs ΔK curves similar to the experimental data collected to date [30].

Batch 3 600s hold tests generated different results than the batch 2 tests. For both FCG and CFCG (60s hold), batch 2 and 3 tests coincided well with one another. However, for the 600s hold time, batch 3 material had drastically higher crack growths rates in comparison to batch 2 600s hold CFCG and both batch 2 and 3 60s hold CFCG. With respect to FCG in batches 2 and 3, the 600s hold time demonstrated crack growth rates that were at minimum 2 times as fast. Unlike 60s and 600s tests for batch 2, the crack growth rate did not slow at the higher stress intensities; rather, the slope of the da/dN vs. ΔK curve was similar or steeper to the FCG curves.

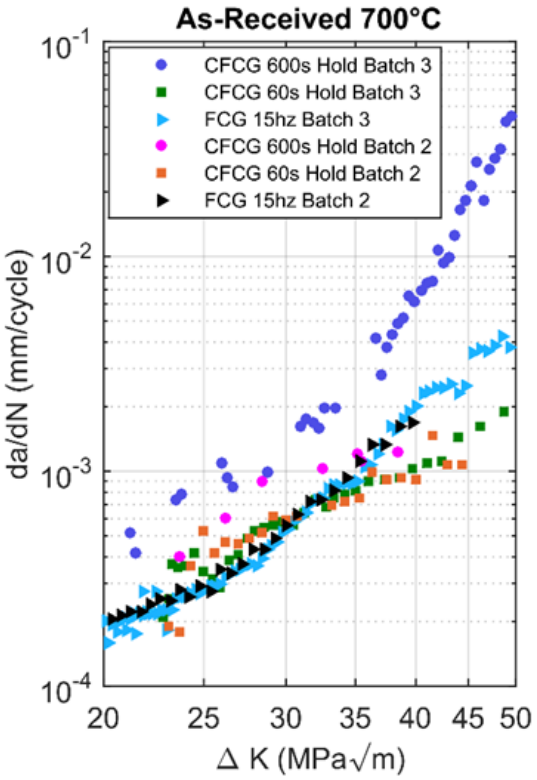

Figure 4.6: FCG and CFCG rates in Batch 2 and 3 material at 700°C

The increase in crack growth rates of batch 3 over batch 2 material is likely a result of increased proficiency with the intermittent loading procedure; however, batch 2 contained a limited quantity of data for valuable conclusions. The intermittent hold time procedure results for the 600s hold times indicate a net increase in growth rate at all ΔK. With crack tip blunting and secondary cracking playing a significant role in the crack growth rates of CFCG it is possible that the intermittent hold procedure created increased crack growth rates during the

600s hold testing intervals. Between CFCG loading cycles, the FCG loading generates a sharp crack tip. If the crack tip blunting plays a significant role in reducing crack growth rates, the sharp crack reformation would likely accelerate the crack growth rate. However, the increased growth rates would appear for a short transient zone where after crack growth rates would stabilize for the tested ΔK. From a $\Delta K \approx 37 MPa\sqrt{m}$ and beyond the tests were conducted as a constant CFCG loading profile without intermittent increases. This suggests that the earlier trend of increased crack growth rates over FCG and CFCG is a result of the 600s hold time and not an artifact of the intermittent hold time procedure. Without running a full length 600s test from start to finish this cannot be verified for the lower ΔK values. The increase in crack growth rates da/dN for the 600s hold suggests that crack growth rates at temperatures of 700°C are time dependent with crack propagation during the hold period. These results are similar to those from Michel et al with 316 and 304 stainless steels [23], and Saxena with P91 in [17]. The time dependence of Alloy 709 is far lower than results found in these studies for 316, 304 and P91.

4.2.2 Fracture Surface (Fatigue/Creep Fatigue Comparison)

Macroscopically, CFCG specimens displayed a much rougher topography than did the FCG samples. Secondary cracking increased overall deformation of the fracture surface. Under CFCG loading profiles, secondary cracking and fracture surface deformation increased with hold time. This increase in topography is especially visible at longer crack length, higher ΔK, as seen in Figure 4.7. Both samples shown, under FCG and CFCG utilized constant amplitude loading over the same stress range.

Comparison of the fracture surfaces between FCG and CFCG with SEM imaging presented numerous surface differences. Fatigue striations were consistently observed at ΔK greater than $25 MPa\sqrt{m}$ at all temperatures tested. Additionally, there was significant secondary cracking observed, particularly at higher ΔK values. For FCG, the secondary cracking appeared to occur both parallel and perpendicular to the direction of crack growth, Figure 4.8a, while the secondary cracks under CFCG appeared predominantly perpendicular to the direction of crack growth, Figure 4.8b. CFCG showed more pronounced secondary cracking and striations than did the FCG and are more apparent at higher magnifications. Figures 4.8c and 4.8d show 1000x magnification at the higher stress intensity range,

$\Delta K \approx 35 MPa\sqrt{m}$. These figures further demonstrate the increase in size and depth of the secondary cracking under CFCG conditions.

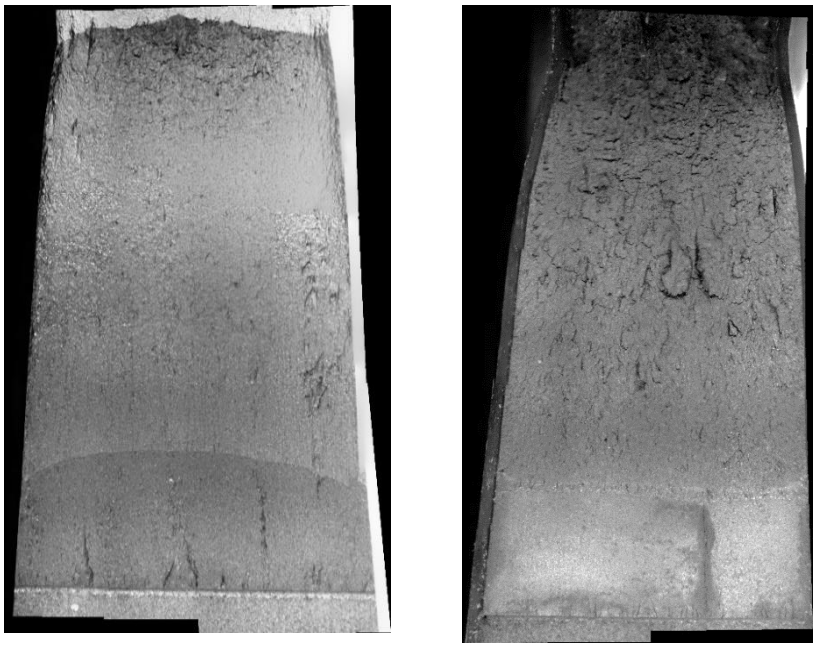

(a) *(b)*

Figure 4.7: Macroscopic fracture surface, Batch 2 Macroscopic fracture surface at 700℃ (a) FCG at a frequency of 15hz, (b) CFCG with hold time of 60s hold

The low frequency FCG (0.01667Hz) fracture surfaces showed similar striation regions as FCG and CFCG. There was a small increase in the quantity of secondary cracking and fracture surface topography as compared to FCG at 15Hz; however, to a lesser extent than CFCG at equivalent ΔK. Figure 4.9 shows striations and secondary cracking of the low frequency FCG in direct comparison to the FCG(15Hz) and CFCG figures previously shown. Crack growth appeared entirely transgranular for all loading conditions.

At 700℃, secondary cracking reduces the driving force at the crack tip and thus reduces the crack growth rate; however, as the hold time increases, the creep zone increases and encompasses the cyclic plastic zone. When fully enveloped within the creep zone, creep crack growth extension occurs during the hold time and secondary cracking from the primary crack plane is insufficient to retard all creep crack extension.

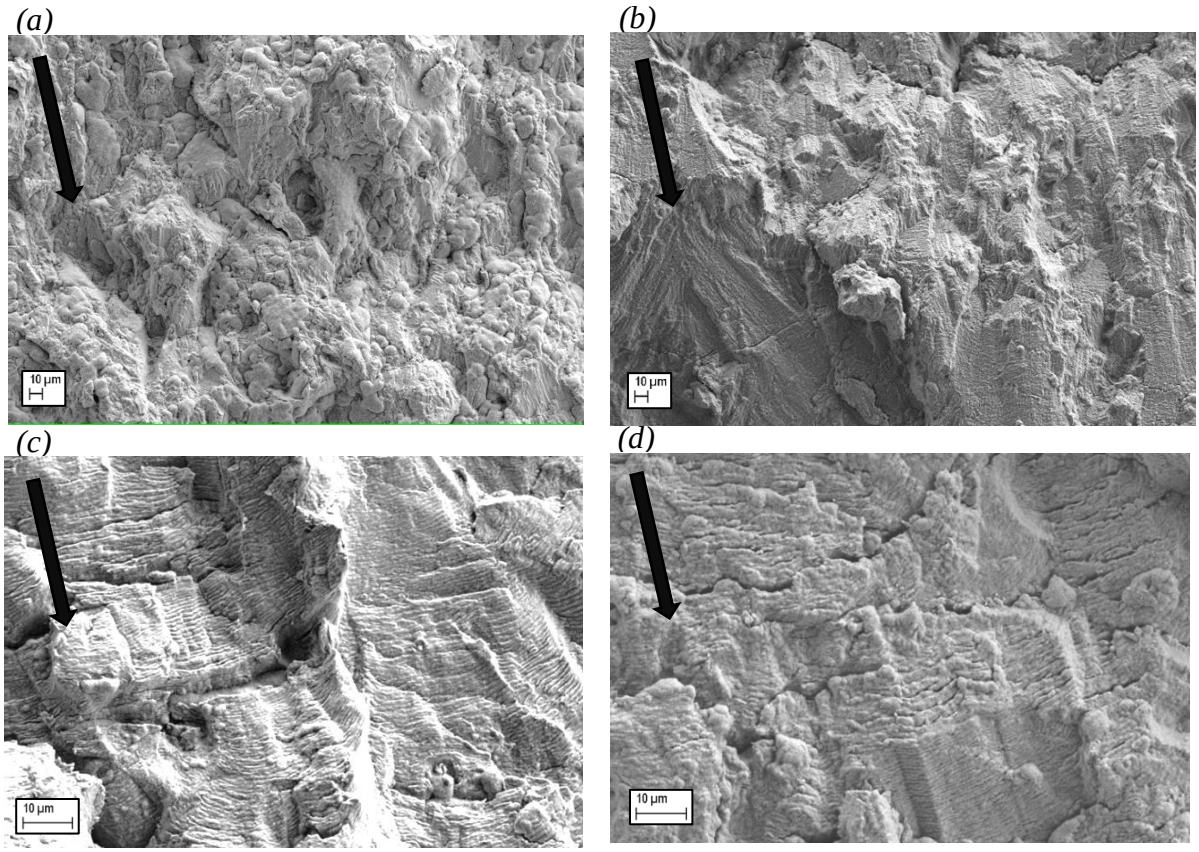

Figure 4.8: (a) FCG, 15Hz, R=0.1 and (b) CFCG 60s hold at 700℃ and ΔK≈25MPa√m at 250x magnification and (c) FCG, 15Hz, R=0.1 and (d) CFCG, 60s hold at 700℃ and ΔK≈35MPa√m at 1000x magnification

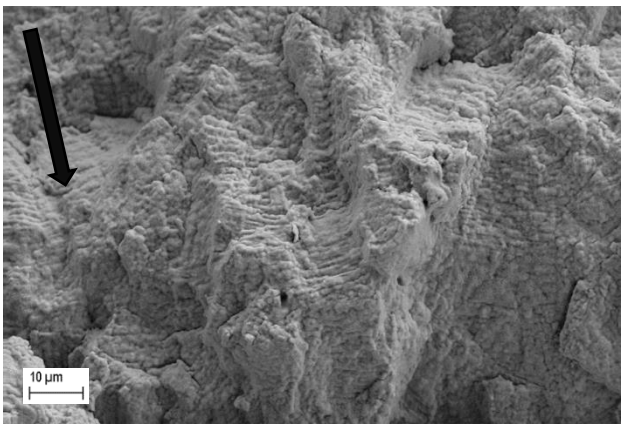

Figure 4.9: FCG (0.01667 Hz) 700℃ , ΔK≈35MPa√m, 1000x magnification

4.2.3 Microstructure/EBSD Scans (Fatigue/Creep Fatigue Comparison)

Metallography was performed on the specimens' post rupture. The CFCG specimen crack profiles have a significant increase in secondary cracks especially at higher stress intensities. Figure 4.10 shows the crack profile of three separate test conditions at equivalent ΔK values of 25 MPa√m. When comparing secondary cracks between FCG and CFCG at this ΔK, larger secondary cracks were evident with CFCG loading profiles along with an increase in additional crack branching from the secondary cracks. This was observed for both 60s and 600s CFCG hold times and predominantly at higher stress intensities (≥25MPa√m). All primary and secondary cracks continued to remain transgranular in nature. The final distinction between the crack profiles and surrounding grain structure is the increase in small grain formation from FCG to CFCG. As the hold time increased at a given ΔK, there was an increase in secondary grain formation. This can be seen in Figure 4.10 as the hold time is increased. The concentration of grain boundaries is increased in c compared to b, and b compared to a.

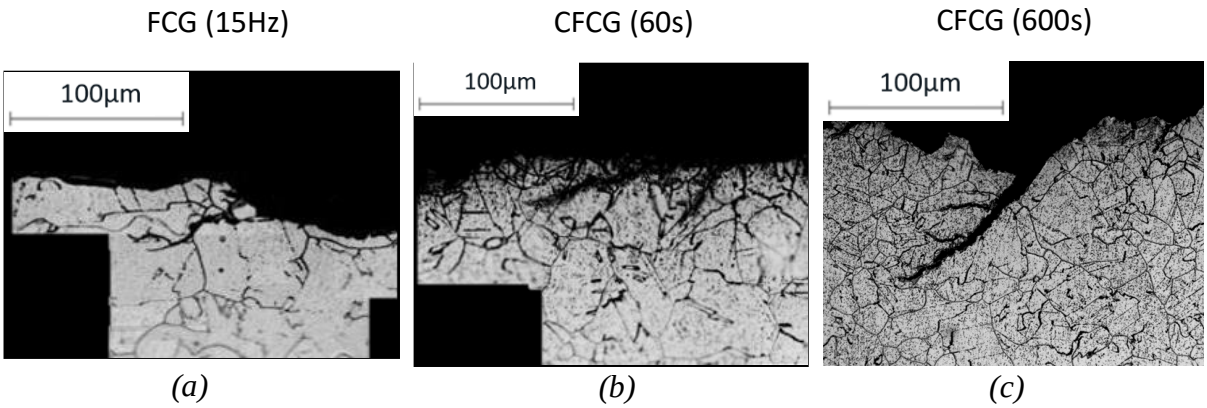

Figure 4.10: Optical Crack Profiles, left to right, (a) FCG(15 Hz), (b) CFCG(60s hold), and (c) CFCG(600s hold) at a ΔK≈25MPa√m

EBSD scans confirm this observation, Figure 4.11, which shows grain boundary misorientation maps of the FCG and CFCG specimens. In these maps, the red concentrations represent low angle boundaries, between 2° and 15° and the black lines show the high angle grain boundaries, greater than 15°. The concentration of low angle boundaries is noticeably greater around both the 60s and 600s CFCG main and secondary cracks in comparison to the FCG cracks. Another important observation from the EBSD maps is confirmation that crack

growth is primarily transgranular, where cracks propagated fully across grains for both the FCG and CFCG samples and not along grain boundaries.

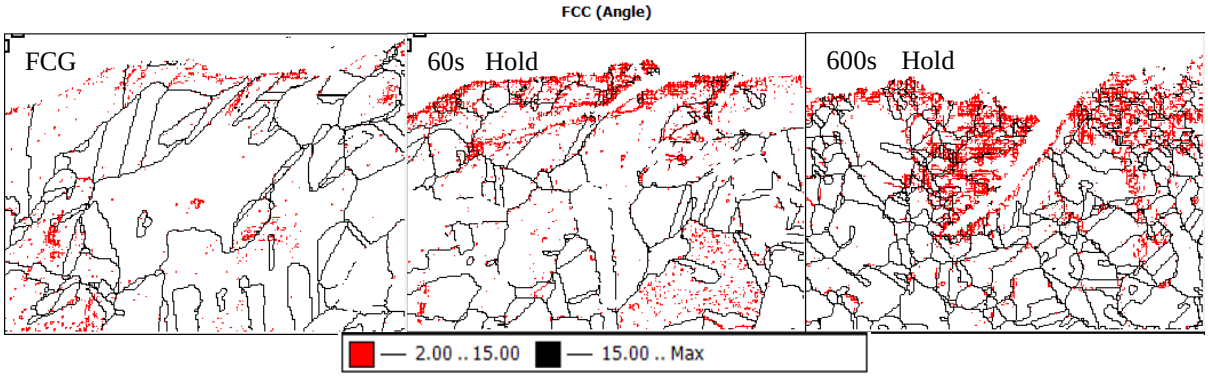

Figure 4.11: EBSD scan grain boundary angles at a ΔK≈25MPa√m: (a) FCG (15 Hz), (b) CFCG (60s hold), (c) CFCG (600s hold)

Figure 4.12 quantifies the concentration of the low angle grain boundaries as a percentage of the total boundary angles recorded. From this figure there is a notable increase in the concentration of grain boundaries 4° and less. From FCG to CFCG the percentage of these low angle boundaries increases from ≈23% to ≈35% while there is a near equivalent decrease in higher angle grain boundaries of ≈60° or greater. From the previous EBSD scans, visually there is an increase in low angle boundaries. When quantified into a percentage of total grain boundaries, the increase in low angle boundary concentration is not as noticeable between the 60s and 600s hold times as there is an overall increase in the quantity of grain boundaries resulting from the increased secondary grain formation. As a result, there are many more grain boundaries in the 600s hold time as compared to the 60s hold time both with small angle grain boundaries and large angle boundaries.

Inspecting the fracture surface and crack profiles, the concentration of low angle grain boundaries remains similar and small grain formation increases between the 60s and 600s hold times. The grain boundary orientation maps show a distinct increase in low angle grain boundaries resulting from CFCG loading profile. The low angle grain boundaries are indicative of new, small subgrain formation and dislocation motion. This formation and dislocation motion are a result of cumulative damage at the crack tip. These EBSD images are in line with the crack growth rates; as the hold time is increased there was an increase in fracture surface damage, yet the overall crack growth rates did not show a great increase.

Overall, this suggests that the increase in damage at the crack surface is dissipating much of the energy at the crack tip outward from the crack plane rather than forward through the crack plane.

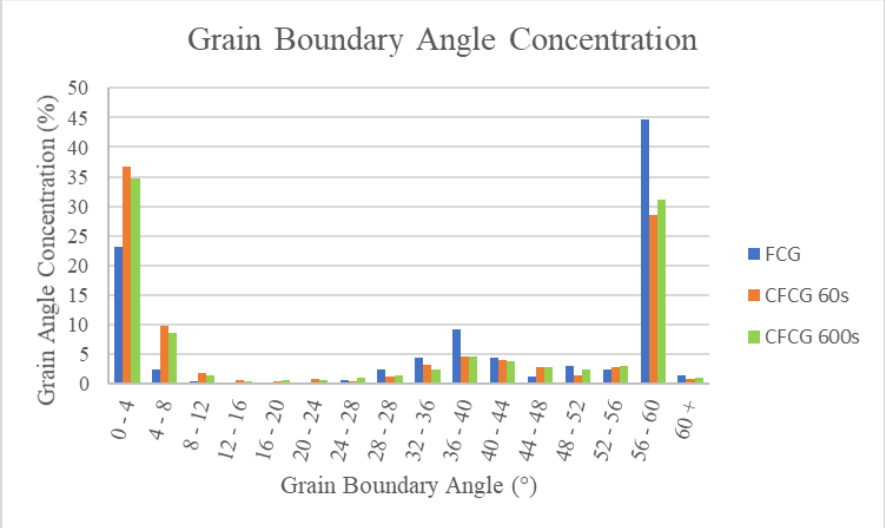

Figure 4.12: Grain boundary angle distribution corresponding to EBSD scans at $\Delta K \approx 25 MPa\sqrt{m}$

4.3 Material Aging Affects

Material aging affects were investigated for both FCG (R=0.1 only) and CFCG (60s hold) conditions. In the as-received condition, four FCG tests were performed at 700°C and three were performed at 550°C. For 60s hold CFCG as-received, two tests were performed at 700°C and one was run at 550°C. In the aged 1 condition, two FCG tests each were conducted at temperature of 550°C and 700°C, and 60s hold CFCG tests were conducted at temperatures of 550°C and 700°C. Finally, in the aged 2 condition, four tests total were performed, one test at each temperature, 550°C and 700°C, for each loading profile, FCG and 60s hold CFCG.

4.3.2 Crack Growth Rates (Material Aging Affects)

Aged conditions of batch 3 had little effect on crack growth rates. For both FCG and CFCG (60s) at 550°C and 700°C, the data fell within a narrow scatter band with a variance of less than a factor 2 throughout the ΔK range. Figure 4.13 presents crack growth data at both 550°C (Figure 4.13a) and 700°C (Figure 4.13b). As seen for both FCG and CFCG, there is only marginal variations in crack growth rate between aged samples without a clear trend for either loading.

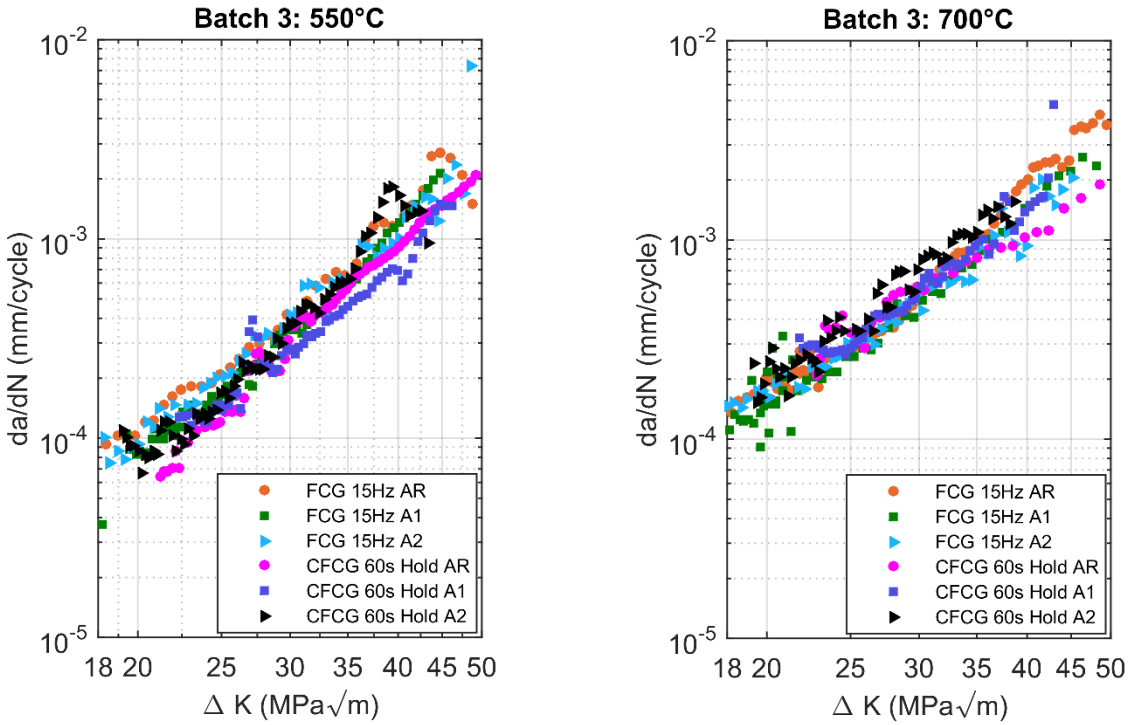

(a) *(b)*

Figure 4.13: Batch 3 aged material comparison, FCG at a 15Hz and CFCG with 60s Hold time: (a) 550°C, (b) 700°C

For both FCG and CFCG loading the data falls within a narrow band. The ageing schedules, 3 months at 650°C and 6 months at 650°C, predicted an increase in the amount of σ phase into the microstructure. Preliminary analysis by the metallurgical department demonstrated a marked increase in strain rates and an increase in σ phase after aging [29]. σ phase is detrimental to the creep strength of stainless steel alloys. From the creep testing conducted, this appears to be the case [29]. For FCG at the tested R-ratio of 0.1 and temperatures of 550°C and 700°C, aging appears to not effect crack growth rates. However, in terms of CFCG (60s Hold) there was an increase in growth rates for the aged 2 condition. The aged 2 condition, at both 550°C and 700°C there was a slight shift in crack growth rates. For both test temperatures, the aged 2 condition crack growth rates were at the upper band of the scatter band for all tests at their respective temperatures. There is an increase in crack growth rate volatility with the aged samples and it is possible that σ phase formation resulted in increased growth rates within sections of the specimen as the aged CFCG tests appeared to have sections of increased scatter for da/dN. From a FCG stand point, there is little evidence

to support that the aged conditions of the material had any effect on the crack growth rates. In contrast to alloys such as 316, Michel et al. showed a decrease in crack growth rates after ageing by nearly a factor of two [23]. Alloy 709 does not exhibit any significant difference in crack growth rate with thermal ageing. The behavior after thermal ageing of Alloy 709 behaves more closely to alloy 304 which demonstrated no effect in crack growth rates from simulated service life conditions [23].

4.3.1 Fracture Surface (Material Aging Affects)

Comparing FCG fracture surfaces at both 550℃ and 700℃ there was little observed difference. Figure 4.14 are representative of the fracture surface of the FCG tests in the as-received, aged 1, and aged 2 conditions. All 3 conditions showed similar fracture surface topography, striations and secondary cracking on the fracture surface when compared at equivalent ΔK regions at 700℃.

Furthermore, comparing the aged conditions for FCG at 550℃, the fracture surface topography, striations and secondary cracking were similar between the batches as at 700℃. At both 550℃ and 700℃ samples displayed striations on the fracture surface that coincided with crack growth rate at any given ΔK; however, secondary cracking was different. At 550℃ secondary cracking had a decrease in depth and overall deformation but an increase in quantity. The increased quantity and decreased depth of secondary cracking is likely a result of work hardening at the crack front. As shown by Upadhayay et al, Alloy 709 work hardens at temperatures below 650℃ [31]. This work hardening effect lends towards the creep-brittle nature of Alloy 709 at the tested temperatures. The fracture surface of the as-received condition at 550℃ FCG loading is presented in Figure 4.15.

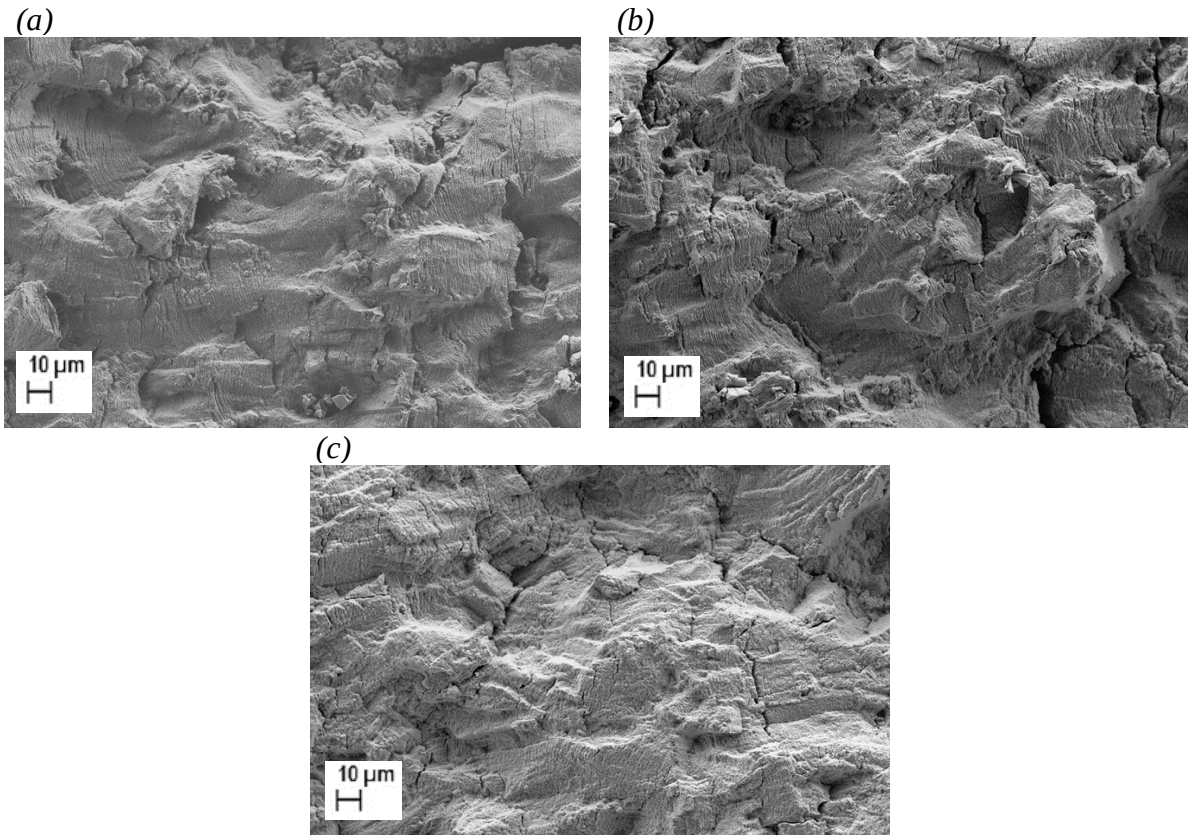

Figure 4.14: FCG 700℃ fracture surfaces, 500x magnification at a ΔK≈35MPa√m, crack growth is right to left (a) as-received, (b) aged 1 condition, (c) aged 2 condition

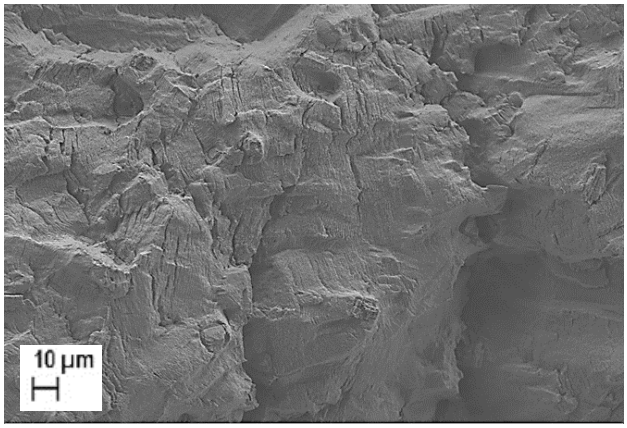

Figure 4.15: FCG 550℃ fracture surface, as-received condition, 500x magnification at a ΔK≈35MPa√m, crack growth is right to left

4.4 R-Ratio Affects

4.4.2 Crack Growth Rates (R-ratio Affects)

Da/dN vs ΔK curves at 550℃ and 700℃ for different R-ratio (0.1,0.3,0.5,0.7) are shown in Figure 4.16. These two plots exhibit typical mean stress effects where higher R-ratios have growth rates faster for a given stress intensity range than lower R-ratios. As ΔK increased the R-ratios of 0.1, 0.3, 0.5, and 0.7 converged. As seen in Figure 4.16 a and b, the higher R-ratios of 0.5 and 0.7 exhibited similar crack growth rates, yet faster crack growth rates compared to R-ratios of 0.1 and 0.3. This trend is also shown in Figure 4.16b for a temperature of 700℃. The primary difference at 700℃ was a decreased difference between the R-ratio curves of 0.1 and 0.3. The R-ratio tests appear to fully merge at a $\Delta K \approx 15$ MPa√m for a temperature of 550℃, Figure 4.16a, and at a $\Delta K \approx 25$ MPa√m for a temperature of 700℃, Figure 4.16b. At 550℃ and at all R-ratios, crack growth rates continued to decrease as the stress intensity was decreased in the near threshold region. The slope of the da/dN vs. ΔK curve at 550℃ is shallower in the near threshold region than at 700℃. At 700℃ crack growth rates decreased rapidly after reaching a crack growth rate of approximately 10^{-5} mm/cycle. The steep slope of the da/dN vs. ΔK curve at 700℃ was observed at all R-ratios. The slope became nearly asymptotic near 10^{-5} mm/cycle, where upon an additional 10^{6} cycles were applied after apparent crack retardation to confirm crack arrest at R-ratios of both 0.1 and 0.5. Although crack growth rates of 10^{-7} mm/cycle were not directly achieved due to the rapid arrest of the crack, threshold stress levels for R=0.1 loading at 550℃ and 700℃ appear to be $\Delta K \approx 7$ MPa√m and $\Delta K \approx 8$ MPa√m respectively. With no apparent crack closure at R=0.7, the ΔK_{eff} threshold stress appears to be $\Delta K_{eff} \approx 4$ MPa√m and $\Delta K_{eff} \approx 6$ MPa√m for 550℃ and 700℃ respectively.

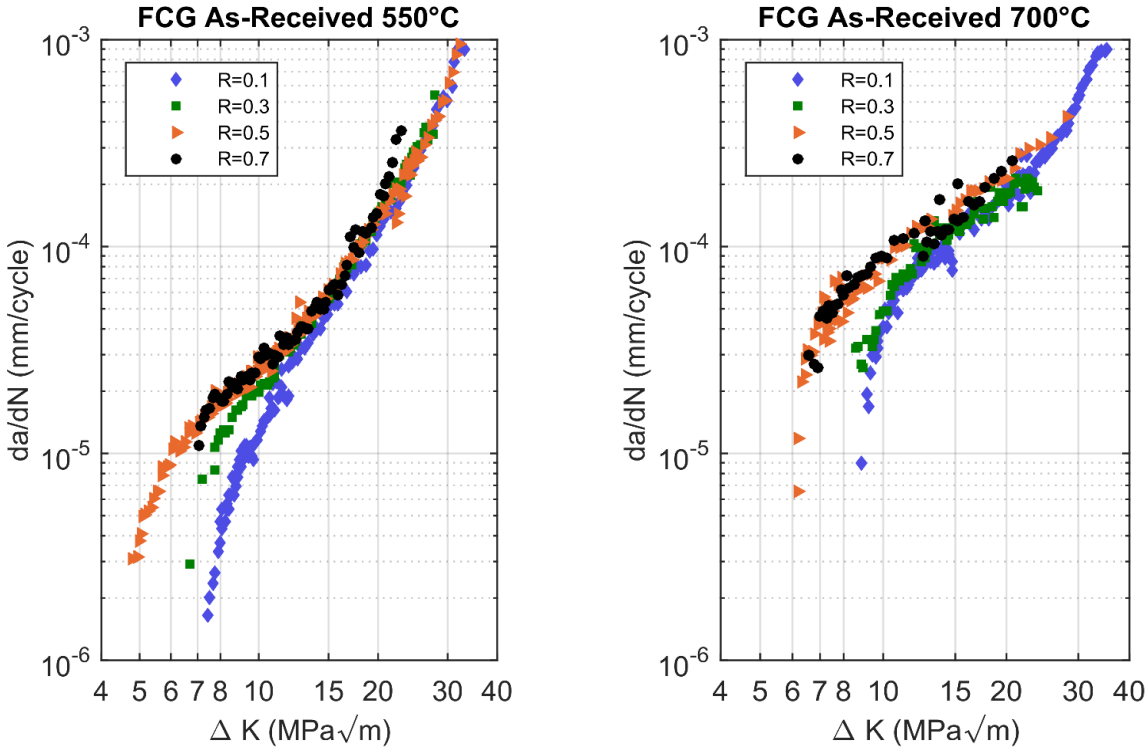

Figure 4.16: FCG at a frequency of 15Hz for Batch 3 material in the As-Received condition at (a) 550°C and (b) 700°C

The data is plotted in terms of ΔK rather than ΔK_{eff}. Higher crack growth rates at low ΔK for R-ratios of 0.5 and 0.7 indicate that crack closure is most likely present at R-ratios of 0.1 and 0.3. Different R-ratios resulted in different crack growth rates in the FCG curves at equivalent ΔK. Growth rates at both 550°C and 700°C showed a decrease in the crack growth rate curves at R=0.1 and R=0.3 relative to R=0.7; however, the difference was less exaggerated between 0.5 and 0.7. At R=0.7, crack closure is likely only present at very low stress intensities or not at all). It is apparent that the R curves merge quickly with one another. At 550°C, all R curves merge by ΔK≈15 MPa√m and at 700°C the curves merge by ΔK≈25 MPa√m. Merging of these curves indicates that crack closure is nearly eliminated at all R-ratios at the respective ΔK. As expected the higher R-ratios of 0.5 and 0.3 merge more quickly than the R-ratio of 0.1. Crack growth data is in strong agreement with current simulation and modeling efforts. Current simulations conducted at the UI utilizing a strip-yield model predict similar opening

loads as the experimental results [32]. The modeling efforts are in agreement with previous work from Wang and Blom [33]

4.4.1 Fracture Surfaces (R-ratio Affects)

Fracture surfaces showed differences between R-ratio loading profiles. At 700℃, differences in the fracture surface are the most pronounced. As R-ratio increased the fracture surface topography and depth of secondary cracking increased. There was an increase in topography and secondary cracking at R-ratios of 0.3, 0.5 and 0.7 compared to R=0.1. The differences are most pronounced between R=0.1 and R=0.7 as seen in Figure 4.17. The increase in secondary cracking depth resulted in increased surface topography that is noticeable microscopically, though to a lesser extent than the 60s hold CFCG loading. At a temperature of 550℃ the same trend of increased topography and secondary cracking develops although the increase was less pronounced. These images are characteristically similar to the fracture surfaces at 550℃ and R-ratios of 0.1 and 0.7.

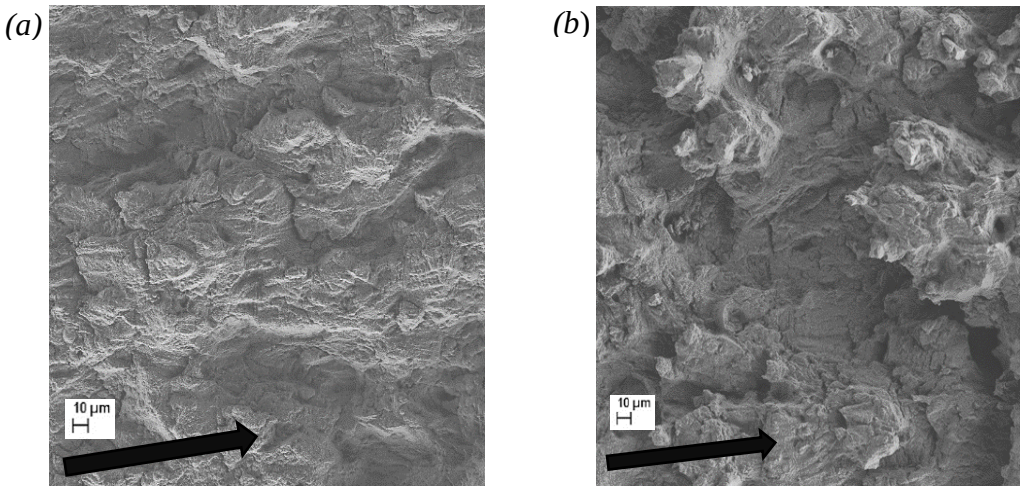

Figure 4.17: Batch 3 As-Received material at 700℃ and ΔK≈25MPa√m and 250x Magnification (a) FCG R=0.1 and (b) FCG R=0.7

Fracture surfaces differences were a direct result of the increased mean and maximum loads applied to the specimen. Similar to the CFCG loadings, the increased time of crack opening resulted in increased fracture surface topography due to increased secondary cracking prevalence and depth. Analysis of the crack plane utilizing EBSD scans would likely result in similar conclusions to CFCG loading; increased R-ratios would result in increased low angle grain boundary concentrations and small grain formation.

5. Conclusions

5.1 Batch variations

Batch 2 and 3 material exhibited similar crack growth rates as one another under both FCG and CFCG Loading profiles. Batch 1 had crack growth rates that differed from batch 2 and 3, where the da/dN vs. ΔK curves for batch 1 had different slopes compared to batches 2 and 3. Batch 3 material had a large variance in grain size and a banded grain structure of smaller and larger grains. Although there were microstructural differences in batch 3, they did not show an appreciable effect on crack growth behavior in Alloy 709. Microstructure of the as-received material for batch 3 was likely a result of a failure in the solution annealing process. Fracture surfaces of both FCG and CFCG between the batches of material were similar except for the presence of an oxide on the early batch 1 and 2 specimens resulting from the new furnace burn in.

5.2 Creep-Fatigue Loading Comparisons

CFCG loading with a 60s hold time showed little effect on crack growth rate at 600℃ and 700℃. At 600℃ there was no effect on crack growth rates with the 60s hold time or slow frequency loading. At 700℃ there was a small change in slope of the da/dN vs ΔK curves with the 60s hold loading. Batch 2 material yielded insufficient results for analysis of the 600s hold time loading. With batch 3 material, the CFCG 600s hold time showed increased crack growth rates in Alloy 709 when tested using the intermittent hold time procedure. Crack growth behavior for CFCG appeared creep-brittle in nature and was characterized in terms of ΔK. When comparing optical and EBSD micrographs, grain boundary orientation shows a distinct increase in low angle boundary and small grain formation with CFCG loading as compared to the FCG. For 60s hold times, small grain formation and secondary cracking serve to absorb much of the driving force at the crack tip during the hold period of CFCG loading and decreases crack growth rates (da/dN) at $\Delta K > 30 MPa\sqrt{m}$ and 700℃. Crack growth was transgranular for both FCG and CFCG. The 600s hold time CFCG loading showed increased crack growth rates over FCG by, at minimum, a factor of 2.

5.3 Material Aging Affects

For both FCG and CFCG (60s Hold) loading profiles, thermal ageing had no substantial effect on crack growth rates. At temperatures of both 550°C and 700°C, da/dN vs. ΔK fell within a narrow scatter band with scatter less than a factor of 2 throughout the full range of ΔK. Alloy 709 reacts to simulated service ageing similar to Alloy 304 when compared to data collected from [23]. Crack growth rates for CFCG at 700°C showed the most volatility in crack growth rates. At both tested temperatures the aged 2 material presented the highest crack growth rates over the as received conditions. Investigating the fracture surfaces between aged specimens showed no difference as a result of ageing regardless of load profile. All fracture surfaces displayed secondary cracking and fracture surface topography consistent with the as received material at the testing temperature.

5.4 R-ratio Affects

Alloy 709 displays typical mean stress effects. Crack closure was effectively eliminated by R=0.7 and potentially as low as an R=0.5. The effect of crack closure diminishes with increasing ΔK and the R-ratio curves merge quickly, at a ΔK≈15 MPa√m for 550°C and at a ΔK≈25 MPa√m for 700°C. The experimental crack growth data generated is in strong agreement with current simulation and modeling efforts, where closure is nearly eliminated by an R-ratio of 0.5. Near threshold data suggests that the threshold ΔK for 550°C is ≈7 MPa√m and at 700°C threshold ΔK is ≈8 MPa√m for an R=0.1. Fracture surface topography and secondary cracking increased with the increased R-ratio loading.

6. Recommendations

The results of this research suggest that Alloy 709 has high temperature strength characteristics that are suitable for nuclear reactor applications. Prolonged thermal ageing of the alloy does not appear to affect the crack growth rates under various FCG and CFCG loading conditions. The CFCG loading with 60s hold times appear to have a negligible effect on the crack growth rates. There is some question as to the longer hold time effects on the crack growth rates. Because of the small sample size and of tests at prolonged hold times, it is advisable to, firstly validate the intermittent testing procedure for this alloy, and secondly, perform more CFCG tests at various hold times to investigate the effects of longer hold times. Microstructurally, analysis of microstructural precipitates should be invested with the batch 3 material to verify the mechanisms causing an increase in crack growth rate at longer hold times.

If characterization of crack growth under CFCG conditions by means of $C(T)_{avg}$ is desirable, precise measurement of crack mouth opening would be required. Load line displacement measurement during hold times, if ample resolution could be achieved, would allow accurate characterization of the growth rates as a function of $C(T)_{avg}$. Accurate measurement of load line displacement would remove uncertainty in the C_{ssc} calculations resulting from uncertain Norton constants A and n.

R-ratio testing at elevated temperatures could yield valuable information in terms of ΔK_{eff} if load line displacement measurements had resolution sufficient to record crack opening with respect to load. The capability to measure with sufficient resolution within the testing chamber would require a high temperature extensometer that has a sufficient clipping force at the specimen mouth to ensure proper measurement and in phase comparison to loading. It would be recommended to analyze the crack plane of the R ratio tests utilizing optical microscopy and potentially EBSD scans for comparison between R ratios.

For increased resolution of the crack length measurement, a switching DCPD setup would offer many advantages. Switching DCPD takes a measurement in both the forward current and reversed current directions. By reading a voltage in both the forward and reverse current orientation and averaging the readings, thermal effects are and overall noise from the current signal would be canceled. Along with switched DCPD, digital information from the multimeter should be sent to the computer via digital RS 232 communication. Current analog

reading of the voltage from the DCPD system increases noise and precision loss through multiple conversions. Additionally, switched DCPD or an ACPD (Alternating Current Potential Drop) would allow for increased environmental testing under different environments or solutions without sacrificing resolution.

References

[1] L. Chengliang and Y. Mengjia, “The Challenge of Nuclear Reactor Structural Materials for Generation IV Nuclear Energy Systems,” p. 8.

[2] F. Delage, J. Carmack, C. B. Lee, T. Mizuno, M. Pelletier, and J. Somers, “Status of advanced fuel candidates for Sodium Fast Reactor within the Generation IV International Forum,” *Journal of Nuclear Materials*, vol. 441, no. 1–3, pp. 515–519, Oct. 2013.

[3] G. Koo and J. Lee, “High temperature structural integrity evaluation method and application studies by ASME-NH for the next generation reactor design,” *Journal of Mechanical Science and Technology; Heidelberg*, vol. 20, no. 12, pp. 2061–2078, Dec. 2006.

[4] S. V. Evropin and V. M. Filatov, “Service-life analysis of nuclear reactor elements under high-frequency random loading,” *Atomic Energy; New York*, vol. 113, no. 4, pp. 258–264, Feb. 2013.

[5] “Sodium-cooled Fast Reactor (SFR) Technology and Safety Overview,” Washington, DC, 18-Feb-2015.

[6] R. Stephens, A. Fatemi, R. Stephens, and H. Fuchs, *Metal Fatigue in Engineering*, Second. Wiley-Interscience, 2001.

[7] “ASTM E647-95a: Standard Test Method for Fatigue Crack Growth Testing.” .

[8] “ASTM E-647.X1: Recommended Data Reduction Techniques.” .

[9] “ASTM E2760-10e2: Standard Test Method for Creep-Fatigue Crack Growth Testing.” .

[10] “MTS | Test systems, simulation systems and load frames.” [Online]. Available: https://www.mts.com/en/products/producttype/test-systems/index.htm. [Accessed: 20-Aug-2018].

[11] “ASTM E-647.A2: Guidelines for Use of Complience to Determine Crack Length.” .

[12] “ASTM E-647.A3: Guidelines for Electric Potential Difference Determination of Crack Size.” .

[13] K. Sadananda and P. Shahinian, “Effect of Environment on Crack Growth Behavior in Austenitic Stainless Steels under Creep and Fatigue Conditions,” NAVAL RESEARCH LAB WASHINGTON DC, NAVAL RESEARCH LAB WASHINGTON DC, Apr. 1979.

[14] K. Sadananda and P. Shahinian, “Prediction of threshold stress intensity for fatigue crack growth using a dislocation model,” *Int J Fract*, vol. 13, no. 5, pp. 585–594, Oct. 1977.

[15] B. Hamilton, D. Hall, A. Saxena, and D. McDowell, “Creep Crack Growth Behavior of Aluminum Alloy 2519: Part 1-Experimental Analysis.”

[16] M. C. Carroll and L. J. Carroll, “Fatigue and creep–fatigue deformation of an ultra-fine precipitate strengthened advanced austenitic alloy,” *Materials Science and Engineering: A*, vol. 556, pp. 864–877, Oct. 2012.

[17] “Crack growth behavior of 9Cr−1Mo (P91) steel under creep–fatigue conditions,” *International Journal of Fatigue*, vol. 56, pp. 106–113, Nov. 2013.

[18] A. Saxena, *Nonlinear Fracture Mechanics for Engineers*, First. CRC Press, 1998.

[19] J. L. Bassani, D. E. Hawk, and A. Saxena, “Evaluation of Ct Parameter for Characterizing Creep Crack Growth Rate in the Transient Regime,” *Nonlinear Fracture Mechanics: Time-Dependent Fracture Mechanics*, vol. 1, pp. 7–29.

[20] V. Kumar, M. D. German, and C. F. Shih, “Engineering approach for elastic-plastic fracture analysis,” General Electric Co., EPRI-NP--1931, 1981.

[21] S. J. Zinkle and G. S. Was, “Materials challenges in nuclear energy,” *Acta Materialia*, vol. 61, no. 3, pp. 735–758, Feb. 2013.
[22] T. Sourmail, “Precipitation in creep resistant austenitic stainless steels,” *Materials Science and Technology*, vol. 17, no. 1, pp. 1–14, Jan. 2001.
[23] D. J. Michel, H. H. Smith, and H. E. Watson, “Effect of Hold-Time on Elevated Temperature Fatigue Crack Propogation in Fast Neutron Irradiated and Unirradiated Type 316 Stainless Steel,” Naval Research Laboratory, Naval Research Laboratory, Washington D.C.
[24] “ASTM E1457-98: Test Method for Measurement of Creep Crack Growth Rates in Metals.” .
[25] “ASTM E466-96: Practice for Conducting Force Controlled Constant Amplitude Axial Fatigue Tests of Metallic Materials.” .
[26] “ASTM E21-92: Elevated Temperature Tension Tests of Metallic Materials.” .
[27] “ASTM E-399.A4: Special Requirements for the Testing of Compact Specimens.” .
[28] P. Malmqvist, “Monitoring of crack growth and crack mouth opening displacement in compact tension specimens at high temperatures,” Karlstads University, 2016.
[29] M. Taylor, “Creep and Microstructural Characterization of Advanced Austenitic Stainless Steel Alloy 709,” Thesis, University of Idaho, 2018.
[30] J. Ramirez, Private Communication.
[31] S. Upadhayay, H. Li, P. Bowen, and A. Rabiei, “A study on tensile properties of Alloy 709 at various temperatures,” *Materials Science and Engineering: A*, vol. 733, pp. 338–349, Aug. 2018.
[32] G. P. Potirniche, “Modeling and Simulation of R-ratio Effects on Alloy 709,” To be Published.
[33] G. S. Wang and A. F. Blom, “Strip model for fatigue crack growth predictions under general load conditions,” *Engineering Fracture Mechanics*, vol. 40, no. 3, pp. 507–533, 1991.

Appendices

A.1 Testing interface/Setup

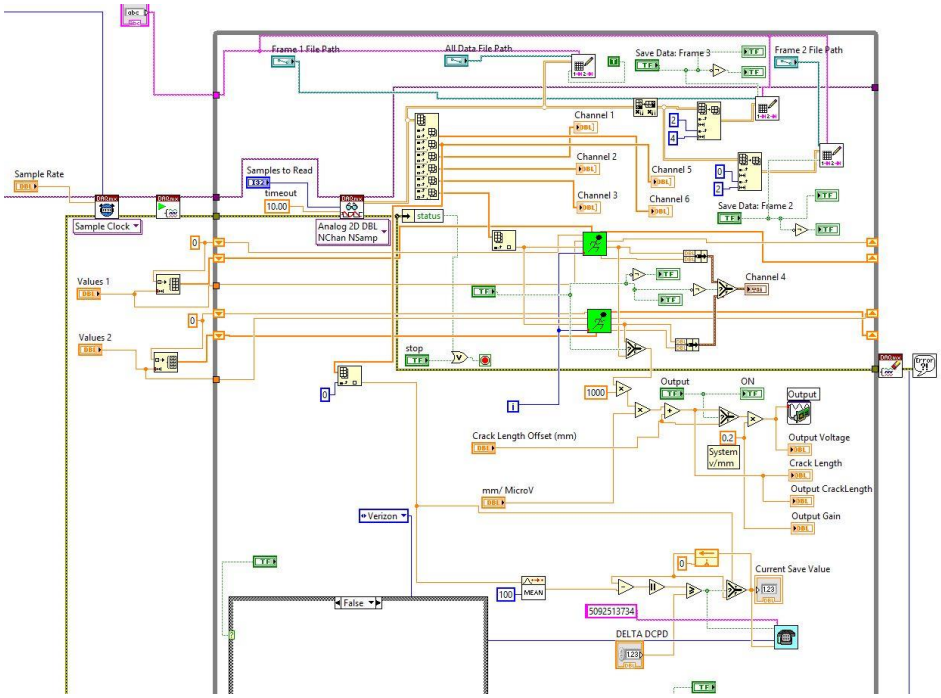

Figure A.1: User interface rear panel for data acquisition

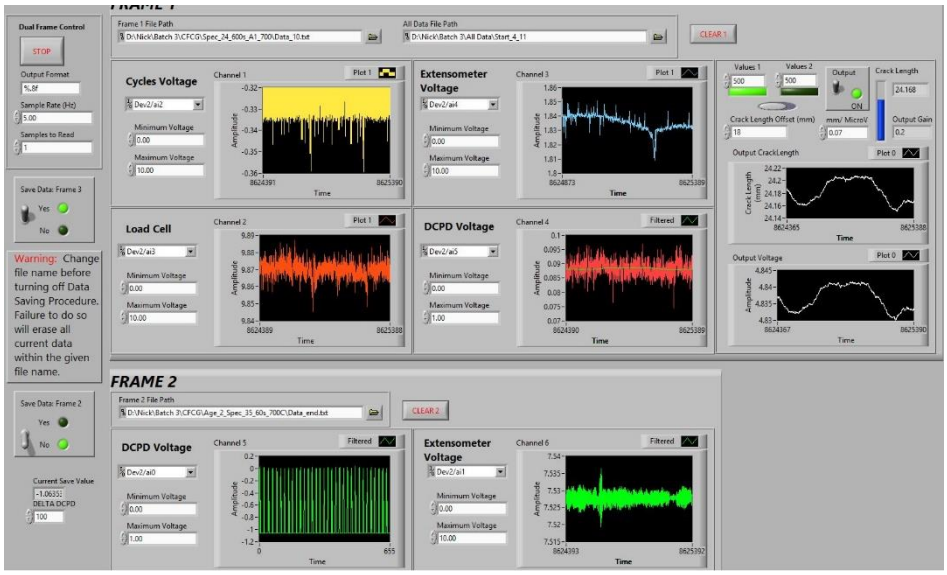

Figure A.2: User interface front panel for data acquisition

A.2 Python Data Reduction

```
for n in range(0,len(Cycle_select_1)-aveval):
    ave_cycles.append((float(sum(Cycle_select_1[n:aveval+n]))/aveval))
    ave_DCPD.append((float(sum(DCPD_select_1[n:aveval+n]))/aveval))
    ave_Length.append((float(sum(Length_select_1[n:aveval+n]))/aveval))
    ave_DeltaK.append((float(sum(DeltaK_select_1[n:aveval+n]))/aveval))
    ave_DeltaK_1.append((float(sum(DeltaK_select_11[n:aveval+n]))/aveval))

Cycle_select = []
DCPD_select = []
Length_select = []
DeltaK_select = []
DeltaK_select_1 = []

print('Done Averaging, Starting Selection of spacing =',a_stepsize,'mm')
t=0
a=0
Cycle_select.append(ave_cycles[t])
DCPD_select.append(ave_DCPD[t])
Length_select.append(ave_Length[t])
DeltaK_select.append(ave_DeltaK[t])
DeltaK_select_1.append(ave_DeltaK_1[t])

while t<len(ave_cycles):
    if ave_DCPD[t] - ave_DCPD[a]>=a_stepsize:
        Cycle_select.append(ave_cycles[t])
        DCPD_select.append(ave_DCPD[t])
        Length_select.append(ave_Length[t])
        DeltaK_select.append(ave_DeltaK[t])
        DeltaK_select_1.append(ave_DeltaK_1[t])
        a = t
    else:
        t+=1
```

Figure A.3: Python data reduction/selection (operated in Jupyter notebook)